



## MASTEARBEIT

# Single-Molecule Analysis of the T Cell Receptor and the $\zeta$ -Chain within the Membrane of T Lymphocytes

Ausgeführt am Institut für  
Angewandte Physik  
der Technischen Universität Wien

unter der Anleitung von

Univ.Prof. Dipl.-Ing. Dr.techn. Gerhard Schütz

Univ.Ass. Dipl.-Ing. Dr.techn. Mario Brameshuber

durch

Benedikt Rossboth, BSc.

Kandlgasse 7/2/10, 1070 Wien

20. August 2015



# Danksagung

Der erste Dank gilt der gesamten Biophysik-Arbeitsgruppe, allen voran Gerhard Schütz, sowie Mario Brameshuber. Danke Mario für die ausgesprochen gute, lehrreiche Betreuung, die auf einer perfekten Abstimmung aus Vertrauen, Motivation, Rat und Kritik basierte. Insbesondere bedanken möchte ich mich noch bei Elena Parkinson für die Assistenz in der Zellkultur, und bei Florian Baumgart für die Unterstützung und Tipps bei den erforderlichen Transfektions- und Transduktionsarbeiten. Ein großes Dankeschön geht auch an die Mauszellen-Lieferanten der MUW, Florian Kellner und Iago Doel Perez.

Natürlich möchte ich mich auch bei meiner Familie bedanken, zuallererst bei meinen Eltern. Mama und Papa, vielen Dank, dass ihr mir den Studienabschluss ermöglicht habt, nicht nur finanziell, sondern auch durch die enorme Kraft, die ich immer wieder bei heimatlichen Kurzbesuchen tanken konnte. Danke, Katharina und Theresa, für die entspannenden, ablenkenden Mittagspausen, Kaffeehausbesuche, gemeinsamen Abende und dafür, dass ich weiß, dass ihr jederzeit für mich da seid.

Danke Sophia, für das vielfache Korrekturlesen meiner Arbeit, aber natürlich noch viel mehr für die unglaubliche Geduld und Unterstützung, nicht nur während dieser Arbeit. Ich freue mich auf alles was noch auf uns zukommt.

# Abstract

The immune system protects an organism in a multitude of different ways. The T lymphocytes, with their respective T Cell Receptor (TCR), bear a grave role by binding foreign antigens and initiating the adaptive immune response. Even though the TCR and its associated proteins, CD3 and  $\zeta$ , are long known to execute this vital task, much remains to be elucidated. The  $\zeta$  chain represents an essential part of the complex for assembly and membrane association, as well as for accurate signal initiation. Most studies on the TCR/CD3/ $\zeta$  complex were made by rather indirect methods, such as co-immunoprecipitation. However, with the recent progress made in light microscopy, enabling single molecule observations, more direct experiments can be done. In this work, single molecule tracking experiments were performed to get information on the diffusional behaviour of some of the involved proteins, i.e. TCR $\beta$  and  $\zeta$ . Furthermore, two-color PALM was used to examine possible clustering of TCR $\beta$  and  $\zeta$  in resting and stimulated primary mouse T cells. The utilized algorithms for localization and tracking were evaluated before use and found to be adequate for densities and SNRs in the range of the actual experiments. The potency of the used murine T cells to induce Ca<sup>2+</sup> flux by pMHC binding was confirmed. Interestingly, the diffusional behaviour of  $\zeta$  was found to differ from the one of TCR $\beta$ , highlighting the possibility of TCR/CD3-free  $\zeta$  within the membrane. These diffusional differences between  $\zeta$  and TCR $\beta$  indicate less stable interactions within the TCR/CD3/ $\zeta$  complex, than identified by biochemical methods. Furthermore, hints on spatial clustering of both proteins were identified. However, crucial pit-falls within a commonly used data analysis on PALM images, i.e. Ripley's K function, were shown.

# Kurzfassung

Das Immunsystem schützt Organismen durch eine Vielzahl verschiedener Mechanismen. Die darin vorkommenden T-Lymphozyten, mit den jeweiligen T-Zell-Rezeptoren (TCR) tragen hierbei eine schwerwiegende Rolle durch das Binden von Peptiden und dem Einleiten der Immunantwort. Obwohl lange bekannt ist, dass der TCR, mit den ihm assoziierten Proteinen CD3 und  $\zeta$ , diese Aufgabe erfüllt, existieren weiterhin einige grundlegenden Fragen. Die  $\zeta$ -Kette stellt einen wichtigen Bindungspartner des TCR dar, und ermöglicht den Zusammenbau des TCR/CD3/ $\zeta$ -Komplexes und dessen Transport in die Zellmembran. Auch innerhalb der Immunantwort übernimmt die  $\zeta$ -Kette wichtige Aufgaben. Die meisten frühen Studien des TCR/CD3/ $\zeta$ -Komplexes basieren auf indirekten, biochemischen Methoden, wie der Co-Immunopräzipitation. Große Fortschritte in der Lichtmikroskopie ermöglichten die Analyse einzelner Moleküle und dadurch direktere Beobachtungen. In der vorliegenden Arbeit wurden Einzel-Molekül-Tracking Experimente durchgeführt, um Information über die Diffusion einiger am Komplex beteiligter Proteine (TCR $\beta$  und  $\zeta$ ) zu erhalten. Weiters wurde 2-Farb PALM durchgeführt, um Informationen über eventuelles Clustering von TCR $\beta$  und  $\zeta$  in ruhenden und aktivierten primären Maus-T-Zellen zu erhalten. Die in der Analyse verwendeten Algorithmen zur Lokalisierung und zum Tracken einzelner Signale wurden evaluiert und als adäquat zur Anwendung an den vorliegenden Bildersequenzen befunden. Die Fähigkeit der verwendeten T-Lymphozyten, durch pMHC-Bindung  $\text{Ca}^{2+}$ -Fluss zu initialisieren, wurde überprüft und bestätigt. Überraschenderweise offenbarte die Diffusionsanalyse Unterschiede in der Diffusion von TCR $\beta$  und  $\zeta$ . Dies weist auf die mögliche Existenz von TCR/CD3-Komplex unabhängigem, Membran-gebundenem  $\zeta$ , und eine weniger stabile Assoziation des TCR-CD3/ $\zeta$ -Komplexes als bisher angenommen hin. Weiters wurden Hinweise auf Clustering der beiden untersuchten Proteine gefunden. Während dieser Cluster-Analyse wurden bedeutsame Nachteile der Verwendung von PALM zu quantitativen Analysen, v.a. durch die Ripley's K Funktion untersucht.

# Contents

<b>1</b>	<b>Introduction</b>	<b>7</b>
1.1	Immunological Background . . . . .	7
1.1.1	The Immune System and Involved Cell Types . . . . .	8
1.1.2	The TCR/CD3/ $\zeta$ Complex . . . . .	10
1.1.3	CD4 <sup>+</sup> T-Cell Activation . . . . .	17
1.1.4	Interactions and Spatial Distribution of T Cell Related Proteins . . . . .	19
1.2	Cell Culture and Transduction of T Cells . . . . .	20
1.3	Light Microscopy and its Limitation . . . . .	22
1.3.1	Super-Resolution Methods . . . . .	28
1.3.2	Single Molecule Tracking . . . . .	31
<b>2</b>	<b>Materials &amp; Methods</b>	<b>35</b>
2.1	Cell Culture and Sample Preparation . . . . .	35
2.1.1	Transformation and Plasmid Preparation . . . . .	36
2.1.2	T-Cell Transduction . . . . .	36
2.1.3	Sample Preparation . . . . .	37
2.2	Laser, Microscopes and Cameras . . . . .	38
2.2.1	SDT 1 . . . . .	39
2.2.2	SDT 3 . . . . .	39
2.3	Image Recording . . . . .	40
2.4	Image Analysis . . . . .	41
2.4.1	Calcium Flux Analysis . . . . .	41
2.4.2	Single Molecule Localisation . . . . .	42
2.4.3	Tracking and Displacement Analysis . . . . .	43
2.4.4	Evaluation of Tracking Algorithm . . . . .	44
2.4.5	Cluster Analysis . . . . .	45

<b>3</b>	<b>Results</b>	<b>49</b>
3.1	Transduction of Primary Murine T Cells . . . . .	49
3.2	Calcium Flux . . . . .	49
3.3	Diffusion Analysis . . . . .	51
3.3.1	Evaluation and Comparison of Tracking Algorithms . . . . .	51
3.3.2	Diffusion Analysis of TCR $\beta$ and $\zeta$ . . . . .	53
3.4	Cluster Analysis . . . . .	54
<b>4</b>	<b>Discussion</b>	<b>61</b>
4.1	Ca <sup>2+</sup> Measurements . . . . .	61
4.2	Evaluation of Localisation and Tracking Algorithm . . . . .	61
4.3	Differences in the Diffusion of TCR $\beta$ and $\zeta$ . . . . .	62
4.4	Apparent Clustering of TCR $\beta$ and $\zeta$ Determined by PALM . . . . .	63
4.5	Further Aspects and Outlook . . . . .	66
	<b>Abbreviations</b>	<b>68</b>
	<b>List of Figures</b>	<b>72</b>
	<b>List of Tables</b>	<b>74</b>
	<b>Bibliography</b>	<b>75</b>

# Chapter 1

## Introduction

### 1.1 Immunological Background

The study of the defensive mechanisms of organisms - immunology - is a comparatively young field. Although references are found within the work of ancient Greek historian Thukydides, mentioning people being resistant against the Plague of Athens in 430BC, the real beginnings of immunology can be dated to the late 18<sup>th</sup> century. It was in 1798, when the English physician Edward Jenner successfully applied vaccination against smallpox for the first time.

Almost a century later, further advances in the field of infectious diseases could be proclaimed. Amongst them, the classification of pathogens - causes of infectious diseases - by Robert Koch, as well as Louis Pasteur's vaccination against cholera, have to be emphasized. Furthermore, the discovery of so called anti-toxins - now known as antibodies - in blood by Emil Adolf von Behring and Shibasaburo Kitasato in 1890, and their effective application to treat diphtheria denotes another finding, which paved the way for modern immunology and got von Behring the Nobel Prize in medicine and physiology in 1901.

With regard to all the manifold diseases emerging from smallest alterations or defects within this protective system, the importance of an organism's intact immune system

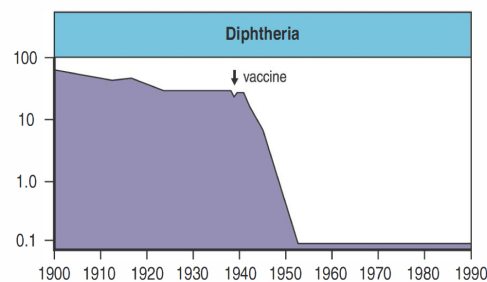


Figure 1: Reported Diphtheria cases per 100.000 people since 1900, demonstrating the impact of the vaccination. Image taken from [1].

becomes clear. The most prominent example might be the Acquired Immune Deficiency Syndrome (AIDS), triggered by the Human Immunodeficiency Virus (HIV) and resulting in a significantly reduced strength of an organism's immune response, transforming typically harmless pathogens into fatal hazards. But not only the absence of particular parts of the immunological machinery contributes to such diseases. Autoimmune diseases, where one's defensive mechanisms against the own immune systems fail, such as Diabetes Type 1, Rheumatoid Arthritis or Multiple Sclerosis - are amongst the ten leading causes of death for women up to 65 years [2].

Within the immune system two different types of responses exist, the innate and the adaptive ones. Innate responses are very fast and thereby enable a successful first defence against an infection without yielding a long-lasting immunity to the respective pathogen. This form of immunity is wide spread over all types of living organisms. However, there are pathogens which cannot be fought by the innate system and the adaptive system comes into play. These responses are developed over an organism's lifetime. Furthermore, this acquired system may develop a memory function, providing a faster and more efficient response for a recurring infection. This system is highly specialised and only found in vertebrates.

### **1.1.1 The Immune System and Involved Cell Types**

#### **Innate versus Adaptive Immune Responses**

The innate immune system is able to respond to pathogens immediately, whereas adaptive immunity requires hours to days to get activated. The efficiency of the adaptive system, however, is very high in contrast to innate immunity. This is caused by different mechanisms of pathogen-recognition in these two systems. The identification by the innate system occurs via pathogen-associated molecular patterns (PAMPs), which are widespread and commonly found molecules in many pathogens (e.g. within the bacterial cell wall), but are absent in the host organism.

The adaptive system, on the contrary, offers a high specificity for pathogens. In the case of initial infection, when the encountering pathogen is unknown, a vast variety of specific receptors has to exist and be ready to be triggered. This is ensured by a mechanism called gene rearrangement, which creates a diverse repertoire of pathogen receptors.

## Selected Cell Types of the Immune System

The cells of the immune system are called leukocytes, or white blood cells, and are derived from pluripotent hematopoietic stem cells in the bone marrow. Within the adaptive system, the class of antigen-specific lymphocytes, i.e. B and T lymphocytes, is involved in almost all actions and is derived from a common lymphoid progenitor cell. The two types of lymphocytes are named after the organ where they mature; B lymphocytes develop within the bone marrow, while T lymphocytes travel as precursors from the bone marrow to the thymus and mature there. In their non-activated, i.e. naive, state, both cell types circulate within the blood and lymphatic system. The initiation of immune responses, however, always occurs in peripheral lymphoid organs comprised of lymph nodes, the spleen and mucosal lymphoid tissues.

The B lymphocytes bind antigens via a specific B Cell Receptor (BCR). Once activated, the cells differentiate to plasma cells and secrete their BCRs as antibodies, also known as Immunoglobulins (Ig). T lymphocytes recognize antigens via TCRs which are closely related to Igs regarding their structure. When activated, they can differentiate to several different sub-cell types. Upon encountering their specific antigen, T lymphocytes alter significantly. Their appearance is changed, with an increased cytoplasmic and nucleic volume and a whole set of new mRNAs and proteins. The cells are then called lymphoblasts and differentiate to varying effector T cells. Those effector lymphocytes either stay in the lymphoid tissue or migrate directly to sites of infection. One type of effector cells are cytotoxic T cells, which kill virally infected cells. There are several different types of helper T cells, e.g. the  $T_{H1}$  cells, which help macrophages to increase their rejection against vesicle-enclosed, intracellular bacteria. However, the term 'helper' T cell originated from the task of supporting B lymphocytes, which is in fact facilitated by the follicular helper cells. Further types of effector cells include the regulatory T cells, which play a crucial role within the adjustment of immune responses, and the memory T cells, which persist after complete extinction of the particular antigen and hence constitute the basis of the immunological memory.

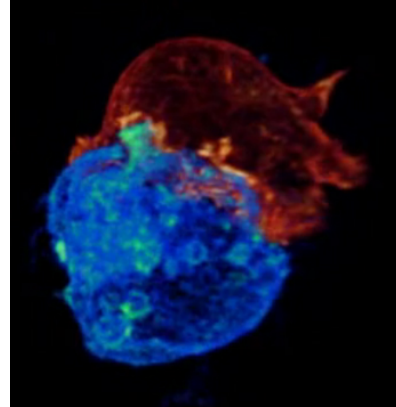


Figure 2: A cytotoxic T cell (red) interacting with a target cell (blue) after establishing an immunological synapse in their interaction surface. Taken from video in [3].

Another important cell type, originally being part of the innate system, are dendritic cells. As mentioned before, the innate system is the first to take action. Whenever these actions are not enough, the adaptive system gets activated. For this purpose, the dendritic cells facilitate the communication between the two distinct immune systems. This is carried out by taking up pathogens, degrading them, and presenting the respective antigens on the cellular surface. Only then, T lymphocytes can recognize those antigens, get activated and initiate the adaptive immune response. For this reason, dendritic cells are also called antigen-presenting cells (APCs).

### 1.1.2 The TCR/CD3/ $\zeta$ Complex

#### Structure of Antibodies

For a better understanding of the T cell receptor and some methods used within this work, the structure of antibodies is now presented more in detail.

The BCR, in its membrane bound form on B lymphocytes, and in the secreted form as antibody, comprises of a variable (V) and a constant region (C) as shown in Figure 3A. The V region is responsible for the great variety amongst antibodies and their high specificity, whereas the C region is only found in five different forms. The purpose of the C region is to perceive the different effector functions in antibodies, while in the BCR, the end of this region is inserted into the membrane. Hence, the BCR has to be associated within the C region with other signalling proteins taking over the initiation of the effector function on antigen binding. One of the five groups is group G (IgG), which represents the largest population of Igs in the body with about 80%.

IgGs are Y-shaped molecules consisting of two heavy (H) and two light chains (L) as shown in Figure 3B. The two H chains, as well as the two L chains are identical within each IgG. In total, the molecular weight adds up to about 150 kDa which corresponds to 2 H chains of 50 kDa each and 2 L chains of 25 kDa each. Both H chains are connected by a disulphide bond, as is one H chain to one L chain, respectively.

The disulphide bonds of IgGs can be cleaved by proteases. Papain, for example, cleaves the bonds between the two heavy chains on the amino-terminal ends, yielding two frag-

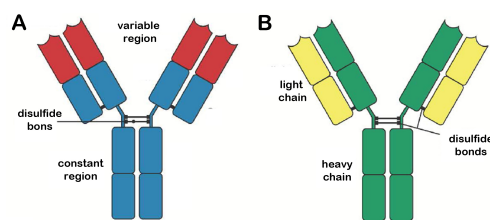


Figure 3: A) The structure of an IgG with the constant region (C) in blue, and the variable region (V) in red. In B) the same structure is shown, but with the heavy chain (H) in green, and the light chain (L) in yellow. Image modified from [1]

ments containing the antigen binding sites on the V region (Fab), and one crystallizing fragment (Fc).

The construction of different Ig-related molecules is enabled by genetic engineering, such as the single-chain variable fragment (scFv) which consists of the V region of an antibody only. As there is no regular linkage between the two parts of the V region *in vivo*, the scFv has to be obtained artificially. The most important benefit of these molecules is their small size, which makes them attractive for different forms of tumour therapy and also makes them, if labelled with a fluorophore, an appropriate fluorescent tracer.

### T Cell Receptor

The structure of antibodies is not only of interest for the production and usage of scFvs and as general labelling and cross-linking molecule, but also, because it resembles the structure of the TCR, which essentially equals a Fab fragment, as well comprising a V and C region. The two distinct chains are termed  $\alpha$  and  $\beta$  chain, instead of heavy and light chain; the V region of the complete hetero-dimeric TCR $\alpha\beta$  is responsible for the high specificity of T lymphocytes against antigens.

Some T cells develop a TCR consisting of two different polypeptide chains resembling the structure of  $\alpha$  and  $\beta$ . Those receptors, called TCR $\gamma\delta$ , have modified properties in antigen recognition, different functions and are limited in number. Within the presented work, the term TCR, however, corresponds to the  $\alpha\beta$ -form.

An important aspect distinguishing the TCR from the antibody structure is the trans-membrane region. In this domain, three basic residues can be found - two in the  $\alpha$  chain and one in the  $\beta$  chain. Those residues undoubtedly play the foremost role in associating with a protein complex called Cluster of Differentiation (CD) 3.

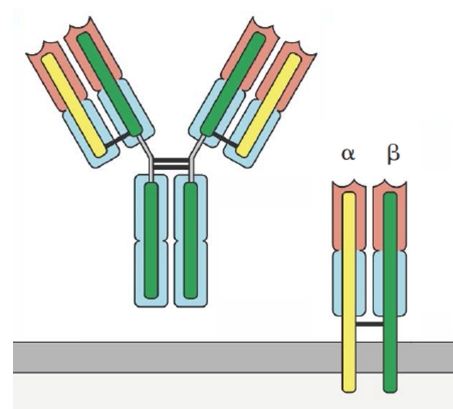


Figure 4: Left) the structure of an IgG, with the same colors as in Figure 3. Right) the structure of the TCR, revealing many shared features. Modified from [1].

## Antigen Binding of T Lymphocytes

B and T lymphocytes differ in their mechanism of binding antigens. Antibodies and BCRs recognize only small parts of pathogens termed epitopes via antigen-binding sites by reversible non-covalent interactions.

The TCR recognizes amino acid sequences, which are often hidden within a protein structure and much shorter than the epitopes recognized by antibodies. This is a reason why the above mentioned APCs are necessary: The dendritic cells internalize pathogens by phagocytosis or endocytosis, break them down by digestive enzymes, and transport them via Major Histocompatibility Complex (MHC) proteins to the membrane. Depending on the origin of peptide digestion (cytosol or vesicular system) the respective class (I or II) of MHCs take over this task. Those peptide-MHCs (pMHC) present the peptide on the outer membrane of the APCs, which enables recognition by a TCR and hence binding of the peptide and initiation of further actions. Class I and class II MHCs are very similar in their structure, with the major differences within the peptide-binding cleft.

There are two different types of co-receptors in T lymphocytes which enhance the response to the binding of pathogenic peptides. They are called CD4 and CD8 (see Figure 5); their expression defines the two major classes of T lymphocytes: CD8 is found on cytotoxic T cells, CD4 on helper T cells. Notably, only CD8<sup>+</sup> T cells recognize and bind to pMHC-I molecules, whereas CD4<sup>+</sup> cells link to pMHCs of class II.

Further molecules, which play crucial roles during the interaction of APCs and T lymphocytes, are the intercellular adhesion molecules (ICAMs) and B7-1 (CD80). All T lymphocytes express an integrin called leukocyte functional antigen-1 (LFA-1), which fa-

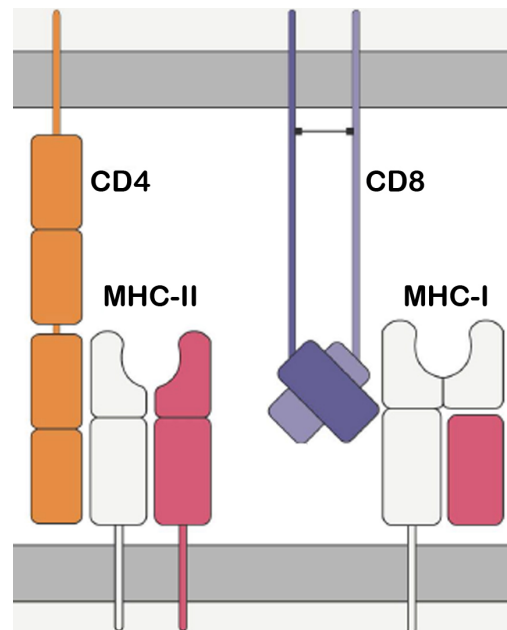


Figure 5: Left) the schematic structure of the co-receptor CD4, present on helper T cells. By its binding to the MHC class II molecule on APCs, such as dendritic cells, B lymphocytes or phagocytes, it facilitates binding of the TCR to the pMHC. Right) the co-receptor CD8 expressed on cytotoxic T cells. It enables the binding of the TCR to the peptide, presented by MHC class I molecules. The MHC-I is expressed on all nucleated cells. Figure modified from [1].

cilitates the cellular migration out of the blood and is important for establishing cell-cell contact. ICAM-1, which is expressed on APCs, binds LFA-1, and thereby strengthens the contact between the cells. B7-1 is a co-stimulatory molecule found on dendritic cells and expressed upon activation via other pathogenic receptors, such as Toll-Like Receptors. By binding to CD28, which is expressed by all naive T cells, B7-1 supports the activation of T lymphocytes.

## Gene Rearrangement, Clonal Selection and T Lymphocyte Development

The great variety of TCRs is provided during lymphocyte development via a mechanism called gene rearrangement, where different separated gene segments are randomly recombined. For a  $TCR\alpha\beta$  V region, multiple copies of three (V, D, J) gene segments can contribute. In total about six million different TCRs can be produced via this gene rearrangement mechanism. An additional mechanism called junctional diversity - the very inaccurate process of connecting the different

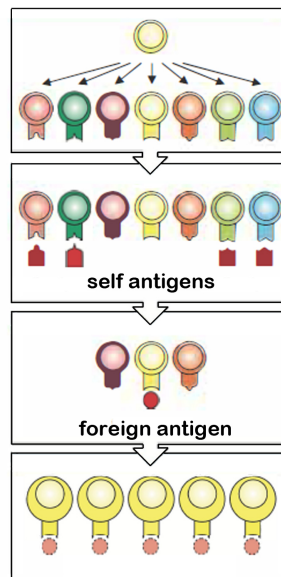


Figure 6: Clonal Selection Theory: Starting from the top, the different stages of clonal selection are shown.

First, a single lymphoid progenitor cell develops into many different T lymphocytes with different specificities. The self-reactive T cells are then eliminated by clonal deletion, yielding mature, naive T cells. When encountering their specific antigen, the T cell proliferates and differentiates. This is then called the clonal expansion. Modified from [1].

gene segments - enables the production of another  $10^{11}$  versions of the TCR, yielding a variety of  $10^{18}$  TCRs.

In a next step, the pathogen-specific antibodies have to be identified and kept, while the non-specific or self-reactive ones have to be depleted. This is performed by clonal selection as shown in Figure 6, where the self-reactive pre-mature lymphocytes are eliminated. The cells recognizing an antigen are selected and enriched via clonal expansion. Importantly, all cells arising from such a selected lymphocyte carry structurally identical receptors, and have thus identical antigen-specificity.

There are three main markers for the developmental stage of T lymphocytes: i) the rearrangement of the genes for the  $\alpha$  and  $\beta$  chains of the TCR, ii) the surface expression of the TCR itself, and iii) the expression of the previously mentioned CD4, CD8 and CD3,

which enables the TCRs signalling functionality. When the progenitor T cells reach the thymus, neither are their genes rearranged nor is TCR/CD3, CD4 or CD8 expressed on their surface. Due to the lack of CD4 and CD8 expression, these cells are called double negative. In this stage, the genes of the TCR $\beta$ -chain are rearranged. The  $\beta$ -chain then assembles with a pre $\alpha$ -chain to the preTCR complex, which is, together with CD3, expressed on the cellular surface. Notably, a dimerization of the preTCR complexes was reported [4]. When the preTCRs are successfully expressed on the membrane, the  $\beta$ -gene rearrangement stops, and CD4 as well as CD8 start to be expressed. This stage is therefore called double positive, and the majority of T lymphocytes within the thymus are in this state. Finally, the genes for the  $\alpha$ -chain start to be rearranged, and low levels of TCR are expressed. Most of those cells, however, fail the positive selection, where non-reactive lymphocytes are eliminated. In case of overcoming this, and the following negative selection, the expression of either CD4 or CD8 stops, the cells become single positives and are ready to be exported. The whole maturation process is estimated to take approximately 3 weeks in mice.

### **TCR/CD3 Complex**

The  $\alpha\beta$ TCR itself has no intracellular signalling motifs; hence, the initiation of signalling processes is not possible. This task is completed by an associated multi-complex protein called CD3, which provides a total of ten Immunoreceptor Tyrosine-based Activation Motifs (ITAMs) to the TCR. Due to the lack of high-resolution structures of such intact complexes, the existing models are mostly based on stoichiometric ratios of the subunits, atomic-resolution structures of folded domains, and biochemical data.

The first detailed finding in the analysis of the TCR/CD3 complex was the detection of two CD3 $\epsilon$  molecules per complex ([5], [6]), followed by the observation of a CD3 $\delta\epsilon$  and a CD3 $\gamma\epsilon$  heterodimer incorporated in the complex [7]. The same biochemical methods revealed one  $\alpha$  as well as one  $\beta$  chain of TCR within intact complexes. However, a dispute remains regarding this monovalency of the TCR, as a second  $\alpha\beta$  heterodimer would result in a net charge of the TCR/CD3 complex of zero. Indeed, some experiments, including Förster Resonance Energy Transfer (FRET) and co-immunoprecipitation suggest the presence of two or more  $\alpha\beta$  heterodimers ([8], [9]). This bivalency is also found in other receptors, such as the erythropoietin receptor [10], which was used to show the possibility of TCR $\alpha\beta$  dimerization [11]. Furthermore, Blue Native-Polyacrylamide-Gel electrophoresis experiments showed a mixture of mono- and multivalent TCR/CD3

complexes extracted from T cell membranes [12]. An additional molecule present in the TCR/CD3 is the  $\zeta$ -chain, also known as TCR $\zeta$ , CD3 $\zeta$  and CD247, a homo-dimer ( $\zeta\zeta$ ,  $\zeta_2$ ) within the complex, detected via biochemical detergent extraction [13].

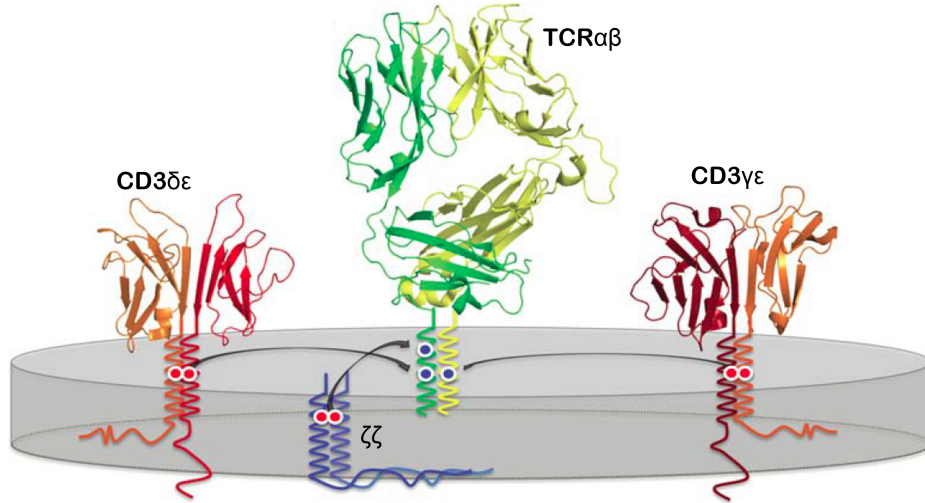


Figure 7: Structure and Interactions of the TCR/CD3/ $\zeta$  complex. The three basic residues within the  $\alpha\beta$ TCR transmembrane domain are represented as blue points, with their respective interactions with the negative charges present on each of the CD3 molecule and  $\zeta$ . The small size of the  $\zeta_2$ , due to its missing extracellular domain becomes apparent. Modified from [14].

Notably, all above mentioned units of CD3 possess a negative charge within their transmembrane domains. As described earlier, the  $\alpha\beta$ TCR has three highly conserved basic residues in this domain, whereby two are located within the TCR $\alpha$ , interacting with CD3 $\delta\epsilon$  and  $\zeta\zeta$ , and the third one is located in the TCR $\beta$ , interacting with the CD3 $\gamma\epsilon$ . But not only those residues seem to be crucial for the assembly and stability of the TCR/CD3, as there are other highly conserved parts found in the different molecules ([15], [16]) and mutational studies revealed influences of the extracellular  $\zeta$  domain [14] as well as the extracellular constant domains of TCR $\alpha$  and TCR $\beta$  ([17], [18]). The interactions within the heterodimers  $\gamma\epsilon$  and  $\delta\epsilon$  are located primarily within their stalk regions, on the extracellular side, just beyond their transmembrane domain ([19], [20]). The  $\zeta$  dimer, on the contrary, is disulphide-linked within its transmembrane domain ([7], [21], [22]). Those interactions between the TCR and the CD3 not only stabilize the complex within the membrane, but also play a crucial role in its assembly as they suppress signals for degradation of unassembled parts ([21], [23]).

The TCR assembly starts in the Endoplasmic Reticulum (ER) by the formation of separate  $\zeta_2$  and TCR $\alpha\beta$ . A TCR/CD3 missing the  $\zeta$  chains is assembled [24], and completed at the trans-Golgi. Almost all synthesized single TCR $\alpha,\beta$ , as well as CD3 $\gamma,\delta$  and  $\epsilon$  molecules are there degraded within 4 hours, whereas  $\zeta$  shows a half-life of 10-20 hours [25]. The hexameric  $\zeta^-$  TCR/CD3 complexes were shown to be transported to lysosomes followed by degradation [26]. The complete complexes are modified within the pre-Golgi, and reach the cell membrane only if folded correctly [27].

The greatly reduced membrane expression of TCR/CD3 complexes in the  $\zeta^-$  deficient cell-line 2B4.11 with returning expression after transfection with a full length  $\zeta$  cDNA, highlights the importance of  $\zeta$  for full TCR/CD3 assembly, surface expression [28] and lifetime enhancement [29]. However, the observation of TCR/CD3-independent  $\zeta$  within the membrane, led to the suspicion of additional complexity in assembly [30].

### The $\zeta$ -Chain

The homodimeric  $\zeta_2$  is of great importance for a functional T cell receptor, and therefore a functional adaptive immune system. This is underlined by the fact that a non-mammalian  $\zeta$  chain is able to restore a fully functional TCR/CD3 complex in mammals [31].  $\zeta$  harbours two known main functionalities: i) it provides six out of ten ITAMs to the complex, and ii) it enables the transport of the complex to the membrane. Fail-

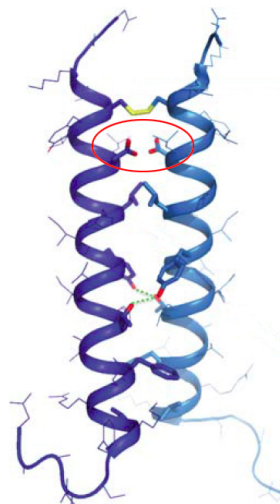


Figure 8:  $\zeta$  homodimer structure as determined by Nuclear Magnetic Resonance Spectroscopy. The critical interactions for dimerization can be seen as well as the aspartic acid pair necessary for TCR assembly (encircled). Modified from [14].

ures or deficiencies in the expression of  $\zeta$  are shown to be involved in many different diseases, such as Multiorgan Tissue Inflammation [32], Systemic Lupus Erythematosus [33] and different types of cancer ([34], [35]).

Notably, the CD247 gene encoding the  $\zeta$ -chain is located on chromosome 1, whereas all other CD3 components are encoded within 300kb of each other on chromosome 11 [36]. The structure of the  $\zeta$  homodimer differs from the other CD3 components as it lacks a significant extracellular domain. This only nine amino acid long sequence, however,

is well preserved, and an artificial enlargement affects the TCR/CD3 complex assembly, and yields super-competent complexes [37]. The presence of a lysine residue at the extracellular position 9 is important for intact signalling, whereas a positive charge on this particular position is necessary for TCR/CD3 assembly, no matter by which amino acid it is provided [38]. This  $\zeta_2$  is one of four known dimeric modules enabling signalling for receptors, as is the Fc receptor  $\gamma$  that is associated with a set of receptors found on Natural Killer cells [14]. All of those have a pair of aspartic acids - which is necessary to connect to their receptors - in their transmembrane domain and share several additional features, such as a common dimerization motif [39].

The  $\zeta$  chain which plays a crucial role in TCR/CD3 surface expression, experiences a rapid turnover within the membrane, independent from the other TCR/CD3 components. This enables an autonomic way of transportation and association-dissociation dynamics for the  $\zeta$  chain [30]. Immunoblotting identified the cell-surface-expressed  $\zeta$  as the only component of the TCR/CD3 complex associated with the cytoskeleton [40].

### 1.1.3 CD4<sup>+</sup> T-Cell Activation

The co-receptor CD4 enables the T lymphocytes to recognize and bind their specific pMHCs.

Different mechanisms how the cell transfers this extracellular binding event into the intracellular milieu are proposed. Most of them are based on molecular clustering ([41], [42]), cooperative binding [42], rapid sub-sequent rebinding [43] and/or mechano-transduction ([44], [45], [46]). In any of these cases, the earliest intracellular action observed is the phosphorylation of the ITAMs present on CD3 and  $\zeta$  via a CD4-associated kinase, the lymphocyte-specific protein tyrosine kinase (Lck).

The ITAMs present on  $\zeta$  are positively charged and are, due to the abundance of the negatively charged phosphatidylserine on the inner leaflet of the membrane, believed to be coupled to the membrane, instead of floating freely within the cytoplasm [14]. In this membrane-associated state, the cytosolic part of  $\zeta$  was shown to be refractory to phosphorylation [47]; hence, a folding transition prior to this phosphorylation has to occur and needs to be initialized by pMHC-binding.

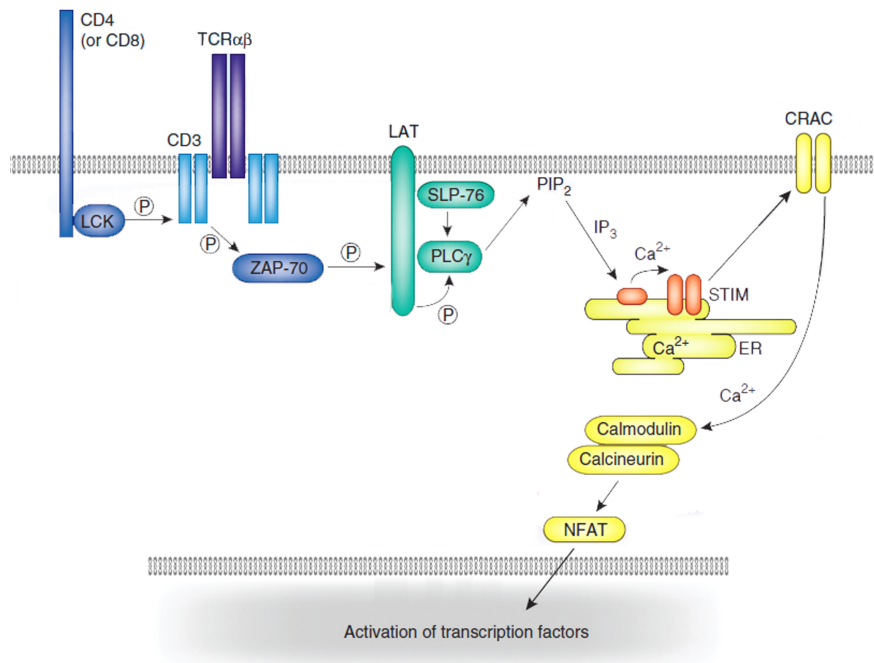


Figure 9: T cell activation pathway containing the intracellular  $\text{Ca}^{2+}$  increase. CD4/CD8 associated Lck phosphorylates the ITAMs present on CD3/ $\zeta$ , followed by phosphorylation of ZAP-70. ZAP-70 phosphorylates LAT and SLP-76. Together they bind PLC- $\gamma$ , which breaks PIP<sub>2</sub> into IP<sub>3</sub> and DAG. IP<sub>3</sub> binds to STIM receptors on the ER, releasing  $\text{Ca}^{2+}$  into the cytoplasm. The free  $\text{Ca}^{2+}$  binds to CRAC in the cell membrane, allowing further  $\text{Ca}^{2+}$  to enter the cell. Calmodulin binds  $\text{Ca}^{2+}$  and acts on Calcineurin, activating NFAT, enabling the transport into the nucleus, and the initiation of transcription of cytokines. Modified from [48].

The  $\zeta$ -chain-associated protein kinase 70 (ZAP-70) can bind to the phosphorylated ITAMs of  $\zeta$  (and CD3) and ZAP-70 then, itself, is phosphorylated by Lck. The active ZAP-70 then phosphorylates the Linker of activated T cells (LAT) as well as the SH2 domain-containing leukocyte protein of 76kDa (SLP-76), which both bind the phospholipase C- $\gamma$  (PLC- $\gamma$ ). The activation of PLC- $\gamma$  results in the breakdown of the intramembranic lipid phosphatidylinositol 4, 5-bisphosphate (PIP<sub>2</sub>) into diacylglycerol (DAG) and inositol 1, 4, 5-triphosphate (IP<sub>3</sub>).

Three separate pathways of T cell activation proceed, all resulting in the regulation of different transcription factors, leading to cell proliferation and differentiation. As  $\text{Ca}^{2+}$  flux experiments are performed in this work, only the pathway resulting in an increased intracellular  $\text{Ca}^{2+}$  concentration will be described:

IP<sub>3</sub> diffuses away from the membrane and binds receptors on the ER, which act as  $\text{Ca}^{2+}$ -channels and release calcium from the ER into the cytosol. Calcium Release-Activated Calcium Channels (CRAC channels) within the cellular membrane are opened and allow

extracellular calcium to enter the cell, yielding a further increase in intracellular calcium levels. Calmodulin binds calcium and targets a phosphatase called Calcineurin, which itself acts on the Nuclear Factor of Activated T-cells (NFAT). This factor initiates the transcription of e.g. a cytokine called Interleukin-2 (IL-2), which plays a major role in strengthening the immune response by initiating the proliferation and differentiation of B- and T-Lymphocytes, as well as of Natural Killer cells.

Not only intracellular pathways are launched by T cell activation, but also increased clustering within the membrane has been observed. Most importantly, after pMHC-binding, micro-clusters of TCR/CD3 complexes, visible even in the diffraction-limited microscope, begin to form. Those micro-clusters are transported to the center of interaction between the T cell and the corresponding APC. Over time, a central Supramolecular Activation Cluster (cSMAC) consisting of different molecules, such as CD4/CD8 and Lck, develops. Other molecules (e.g. LFA-1) are restricted to the peripheral Supramolecular Activation Cluster (pSMAC) surrounding the cSMAC ([49], [50]).

#### 1.1.4 Interactions and Spatial Distribution of T Cell Related Proteins

The event of extracellular ligand-binding and its transmission to the intracellular milieu, initiating T cell activation, is still to be elucidated. Most of the models proposed so far include spatial (re)distributions of involved proteins. First advances into this direction were made by rather indirect, mainly biochemical methods. The variety of methods for more direct observation increased in recent years, not only due to the rising of Single Molecule Localization Microscopy (SMLM). Some of the questions still to be answered are, e.g. the valency of the TCR complex, the full stoichiometry of a TCR/CD3 complex, and possible (pre)clustering of almost all immunological relevant proteins.

Furthermore, the interaction kinetics between  $\zeta$  and the TCR/CD3 complex is still to be characterised, particularly, because  $\zeta$  is often used as a probe for the TCR (e.g. [51]). However, it is questionable, how stable this association of  $\zeta$  to the TCR really is. The membrane expression of  $\zeta$  in the TCR $\beta$ -deficient Jurkat cell line J.RT3-T3.5 highlights the possibility of TCR-independent  $\zeta$  within the membrane [30]. The faster recycling of  $\zeta$  within the TCR/CD3/ $\zeta$  complex indicates the possibility of an autonomous pathway for  $\zeta$  from the Golgi to the membrane [30].

To derive a complete image of the associations of membrane proteins, also their dynamics have to be taken into account [52], especially as some experimental methods are biased towards the detection of either immobile or mobile fractions.

In this work, the association and dynamics of TCR $\beta$  and  $\zeta$  were studied via tracking experiments (Single Molecule Tracking (SMT) and single particle tracking Photoactivatable Localization Microscopy (sptPALM)). (spt)PALM images of  $\zeta$  were acquired, while simultaneously tracking single molecules of TCR $\beta$ . Furthermore, two-color-(spt)PALM images of  $\zeta$  and TCR $\beta$  were recorded.

In 2006, Lillemeier et al. showed clustering of some membrane proteins within cholesterol-enriched, actin-connected protein-islands, using transmission electron microscopy [53]. They confirmed this clustering in 2010 by using PALM: in particular  $\zeta$  and Lat were found in separated clusters containing 7-20 molecules [51]. Clustering of both molecules was further confirmed, and also found for ZAP-70 - with co-localization to  $\zeta$  upon activation - for PLC- $\gamma$ , SLP-76 [54] and Lck [55]. Furthermore, a lipid-dependency for the clustering of Lat was shown [56], connecting these protein clusters with the lipid raft model [57]. Recently, also the clustering of CD4, and its separation from TCR and Lck clusters was observed [58]. Overall, the results of several studies indicate most of the observed proteins to be clustered. The estimated size of those clusters, however, varies between dimers and sizes, large enough to be seen in diffraction limited microscopy [59]. Most studies using SMLM conclude with clusters in the size of 2-30 molecules and an increased size on T cell activation. To examine possible clustering of TCR $\beta$  and  $\zeta$ , (two-color) PALM images were acquired within this work.

## 1.2 Cell Culture and Transduction of T Cells

A huge variety of different cell types is available to investigate cellular mechanisms, such as T cell activation. Different classifications of cells exist, such as, categorizing the cells by their origin and their proliferation characteristics. First, the immortalized cell lines, which under normal circumstances would not proliferate indefinitely, but due to natural or artificially induced mutations do not stop dividing. Second, the primary cells, comprising cells directly gathered from tissues. The primary cells have the restricted lifetime of the respective cells *in vivo* and hence cannot be used after a certain time point.

There is a huge variety of human T-Cell Leukaemia cell lines with different characteristics and lacking the expression of different proteins, such as CD3 or TCR $\alpha\beta$ , as characterized in [60]. One of the most commonly used cell lines in the research of T cell signalling is the Jurkat cell line with its derivatives, e.g. the TCR $\beta$ -deficient J.RT3-T3.5 cell line. Differences in the signalling after T cell activation were found between primary human T cells and T cell lines [61].

By genetic alteration of mice, the production of the huge variety of TCRs can be disabled, and the expression of one type of TCR specific to a desired peptide can be achieved. Therefore, all T lymphocytes produced in such mice show reactivity on antigen stimulation by this specific peptide only. This represents a major advantage for T cell studies and could not be achieved by using e.g. human primary cells. However, the life span of most effector and memory T cells in organisms is comparatively short, limiting the ability to use them for longer time, e.g. for stable transduction [62].

### Transfection, Transduction and Transformation

For fluorescent microscopy experiments, proteins in cells, which are not expressing any fluorescent proteins naturally, have to be made fluorescent. This can either be accomplished by external labelling using e.g. fluorescently-labelled antibodies, or, alternatively, by introducing a foreign plasmid DNA encoding for a fluorescent protein.

All of the terms within this section's title, depict the introduction of external DNA into an organism. While *transfection* is the introduction into an *eukaryotic* organism, *transformation* is the *non-viral* integration into *bacteria or plants*. *Transduction* describes the *viral* incorporation in prokaryotes and eukaryotes.

Primary T lymphocytes are refractory for most DNA delivery methods except electroporation or viral methods. The integration via other methods is mainly aggravated by the low efficiency of available transfection systems and the toxicity of many reagents ([65], [66]).

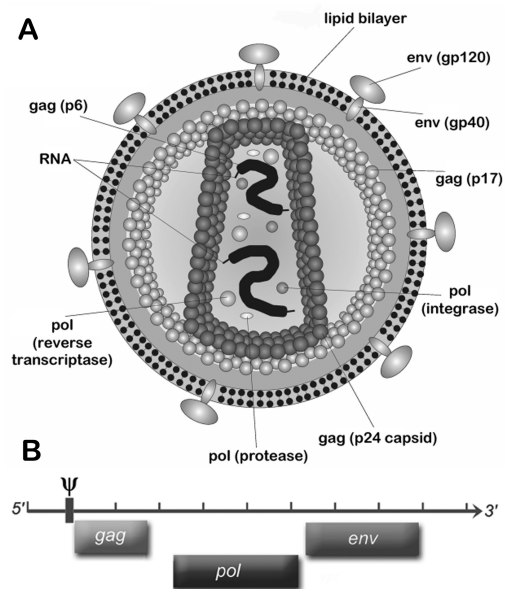


Figure 10: A) Structure and Proteins of a retroviral particle (HIV) modified from [63]. The present proteins, with their respective families are indicated. Those are gp120 and gp40 from the envelope family; p17, p24 and p6 from the gag family and the integrase, the protease and the reverse transcriptase from the pol family. B) Genomic Map of a retrovirus, modified from [64], showing the locations of the genes for the different protein families on a typical retroviral genome.

Retroviral transduction hereby offers the best possibility to introduce foreign DNA into T lymphocytes with a reasonable efficiency [67]. Retroviruses are a family of RNA-viruses with their genetic information available as RNA. Before integrating the RNA into the host's genome, it is translated into DNA via the reverse transcriptase. One famous example of such retroviruses is again the HI virus. Retroviruses comprise of three major protein families: i) gag, a polyprotein responsible for forming the core structure, ii) pol proteins for synthesis and integration of viral DNA and iii) env proteins for the formation of the viral envelope. Another important sequence is termed  $\Psi$ , which signals the packaging of RNA into a viral particle.

The abilities of those three protein families are utilized in packaging cell lines, e.g. the Phoenix line derived by the Nolan lab (Nolan, G., Stanford University, USA, [68]). This line is based on the 293T cell line, which was transfected for expressing the viral proteins mentioned before. The high potential for transfection can further be used to introduce plasmid DNA into those packaging cells. The protein of interest will be expressed and packed into viral particles, which can be utilized for retroviral transduction of other cells, such as T lymphocytes [69].

### 1.3 Light Microscopy and its Limitation

The question arises of how to scrutinize the stoichiometry as well as the interplay of all involved molecules described. Many initial conclusions were based on biochemical methods such as co-immunoprecipitation. However, the recently emerged light microscopy techniques with corresponding increased resolution, even beyond the limitation of diffraction, offer a huge opportunity to get an utterly new point of view on the T cell and its components.

#### History and Basics

It is still a puzzle, whom to credit for creating the first microscope around 1600 as the historical recordings do not allow to decide between the Dutch glass-maker Hans Janssen and his son Zacharias Janssen and the famous Galileo Galilei. However, both microscopes were built by assembling a concave to a convex lens. Huygens then improved the system by adding achromatical correction, hence reducing errors created by different colors, i.e. varying wavelengths, and reached magnifications of up to 50x. In the beginning of

the 17th century, Leeuwenhoek achieved to grind almost spherical lenses and increased the magnification to up to 270x by using only this single lens. It was not until the 19th century, that the physical basics of microscopy were described extensively by Ernst Abbe, and that the first microscope, limited only by the laws of physics and not by constructional constraints, could be created within the laboratories of Carl Zeiss. The basic part of the imaging path of a modern microscope consists of two lenses. In practical use, the object is located at the front focal plane of the first lens, the so called objective lens. An image of the object is generated in infinity. The tube lens captures this light to produce an image at the primary image plane (see Figure 11B).

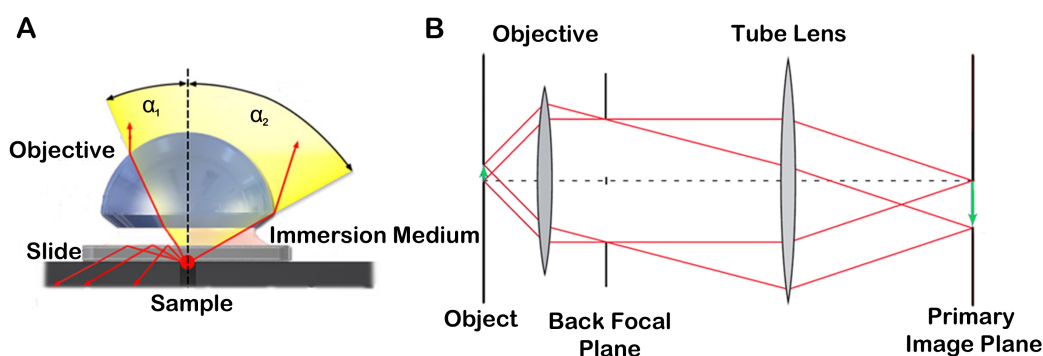


Figure 11: A) Influence of immersion medium on the collection of light, modified from [70]. On the left, no immersion medium is used; light rays with an angle larger than  $\alpha_1$  are refracted at the interface of the glass-slide with air. This angle is increased up to  $\alpha_2$  on the right side, with the use of immersion medium. The refractive indices of the glass-slide and the immersion medium are matched, thus, no refraction occurs on their interface. B) Imaging Path of an infinity corrected microscope adapted from [71]. The light rays originating from the focussed object hit the objective, yielding parallel rays in the space between objective and tube lens. Different optical elements can be introduced here. The tube lens focusses the rays again and creates the image in the primary image plane.

Those systems are called infinity-corrected and one of their advantages is the possibility to insert optical elements, such as filter cubes, within the range of parallel beams. The magnification of such a system is given by the focal lengths of the two lenses:  $M = \frac{f_{tl}}{f_{obj}}$ . When observing a sample directly by eye, the eyepiece of the microscope and the eye lens of the observer represent a second two-lens imaging system, creating a secondary image on the observer's retina. In all single-molecule microscopy systems, the light detection, i.e. image creation, is performed by cameras such as Electron Multiplying Charge-Coupled Devices (EMCCD), skipping this second system of magnification. In addition to the magnification, another important aspect of an objective is the Nu-

merical Aperture (NA) given by

$$NA = n \sin \alpha \quad (1)$$

with  $n$  being the refractive index of the medium in which the sample is prepared, and  $\alpha$  being one half of the objective's opening angle. The  $NA$  characterizes the maximum angle of emitted light which an objective can collect. The angle can be optimized by the use of immersion objectives and immersion media (e.g. oil) between the objective and the glass slide. This adjusts the refractive indices of the varying layers and thus reduces refractive effects on their interfaces (see Figure 11A).

### Fluorescence Microscopy

Some molecules emit light when being illuminated by light of a specific wavelength. This so called fluorescence is taken advantage of in fluorescence microscopy. A simple model describes the molecule in the ground state,  $S_0$ , with reaching an excited state,  $S_1$ , after absorption of a photon. The molecule resides in this state for some hundred picoseconds to nanoseconds, and then either converts to the triplet state,  $T_1$ , or loses its energy and returns via the emission of a photon, to  $S_0$  (fluorescence). Due to intramolecular vibrations and corresponding dissipative energy losses, the energy of the emitted photon is lower than the energy of the initially absorbed one. This shift, called Stokes Shift (Figure 12B), is an essential feature enabling fluorescence microscopy, as it allows to distinguish between excitation and emission light.

As the energy of the emitted photon is lower than the energy of the exciting one, the wavelength will be higher, hence the light will be shifted to the red side of the spectrum of visible light. The model of fluorescence can be depicted using a Jablonski diagram as shown in Figure 12A.

The first of such fluorescent proteins, the Green Fluorescent Protein (GFP), was discovered and extracted from jellyfish in the early 1960s. The ability to fuse this GFP to different proteins made fluorescent investigations possible. Various mutants of GFP, differing in color (Yellow Fluorescent Protein - YFP, photo-switchable Cyan Fluorescent Protein 2 – PS-CFP2, Enhanced GFP - EGFP etc.), were created and a wide variety of fluorophores with very diverse properties exists today.

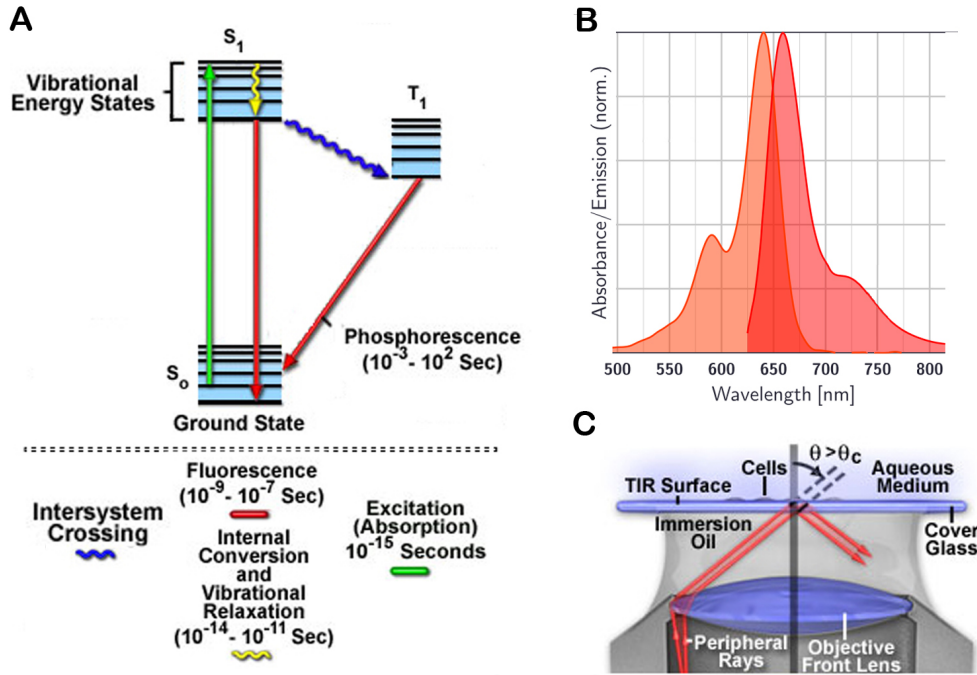


Figure 12: A) Jablonski Diagram, modified from [72]. The fluorescent molecule is excited from its ground state,  $S_0$ , to  $S_1$ . Different vibrational energy states are reached, and the molecule loses energy via internal conversion and vibrational relaxation. The molecule can either lose its energy via fluorescence and directly go back to  $S_0$ , or convert to its triplet state,  $T_1$ , by intersystem crossing, followed by phosphorescence. B) abberior STAR635 spectrum, showing the Stokes shift for fluorescent emission [73]. In orange the excitation spectrum is indicated, whereas in red the shifted emission spectrum is shown. C) Total Internal Reflection Fluorescence (TIRF) excitation modified from [74]. The excitation beam is shifted from the center, and thus, the rays reach the glass slide under a nonzero angle. If the angle is equal to, or larger than the critical angle the rays are reflected totally and only the areas reached by the evanescent wave are excited, yielding a reduction in excitation of out-of-focus background and an increase in SNR.

## Total Internal Reflection Fluorescence

A high Signal-to-Noise ratio (SNR) is of great importance in the field of microscopy. One technique of minimizing background excitation and thus improving the SNR is called TIRF which is based on Snell's law given in Equation 2:

$$n_1 \sin \theta_1 = n_2 \sin \theta_2, \quad (2)$$

with  $n_1$  and  $n_2$  being the refraction indices of the two participating media and  $\theta_1$  and  $\theta_2$  being the two respective angles to the surface normal.

The angle of refraction increases with increasing angle of incidence, if light transits from

a dense optical medium into a less dense one. An angle of incidence exists, where the angle of refraction is exactly  $90^\circ$ . At incidence angles larger than this critical angle, the light is reflected totally.

However, a wave propagating along the surface of transition is generated. This evanescent wave is used in TIRF microscopy to excite only regions within the penetration depth of approximately 100-200 nm. One way to realize this technique is to displace the excitation laser from the center of the objective as shown in Figure 12C.

### Diffraction and Resolution Limitation

Theoretically, additional magnification steps could always be added into a microscopy system, increasing the total magnification. Due to limitations of the resolution, this will, however, lead to no further beneficial effects. Resolution is hereby defined as the ability to resolve two distinct points and can be quantified as the minimal distance between those.

The limitation is ascribed to the wave characteristics of light and two phenomena called interference - the superposition of waves such as electromagnetic waves, i.e. light - and diffraction. Depending on the wave's phase, the intensity of two superimposed waves adds to

$$I(x) = I_1(x) + I_2(x) + 2\sqrt{I_1(x)I_2(x)} \cos[\phi_1(x) - \phi_2(x)] \quad (3)$$

showing that in certain cases, e.g. if the phase difference  $\Delta\phi$  is an odd multiple of  $\pi$ , the resulting wave shows a minimum called destructive interference. For even multiples of  $\pi$ , a maximum called constructive interference occurs as the cosine equals 1.

Christian Huygens formulated a principle of how to determine the path of a light wave, called *Huygens' Principle*, which states that, if the wave front is considered at a certain fixed time point,

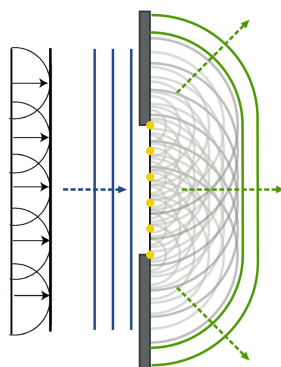


Figure 13: Huygens principle for a plane wave (left). If spherical wavelets are positioned at the beginning of each arrow, the wave front at a later time point, i.e. the end of the arrows, will also be a plane wave. When encountering a single slit (right), the wave front will also reach areas within the geometric shadow of the slit. Figure modified from [75] and [76].

the wave front at a later time point can be derived from placing virtual spherical waves at the actual time point. The sum of the spherical wave fronts represents the wave front at the later time point as shown for a plane wave in Figure 13.

If the light waves pass through a slit with a size in the order of its own wavelength, the light also reaches the border regions behind, which should not be illuminated in geometrical optics. The result of applying the Huygens' principle to a single slit can be seen in Figure 13.

The consideration of interference in the analysis results in a specific pattern, called the Fraunhofer diffraction pattern. A smaller slit results in a larger diffraction pattern. As the rotation of a single slit with constant size yields a circular aperture, the same principles can be applied in this further case. The diffraction pattern of such a circular aperture, or a point object, yields a smeared-out spot, showing a characteristic diffraction profile, called Point Spread Function (PSF) and its analytical derivation, the Airy function.

The minimal size of a single spot in the image plane can be determined by deriving the first minimum of the Airy function. The systems characteristics, i.e. the opening angle of the objective and the refractive index of an immersion medium, have to be taken into account to derive a corresponding distance within the object plane. The minimal size of a single bright spot imaged with a microscope can be calculated by

$$d = \frac{0.61 \cdot \lambda}{n \sin \alpha} = \frac{0.61 \cdot \lambda}{NA}, \quad (4)$$

with  $\lambda$  the wavelength of the light used,  $n$  the refractive index,  $\alpha$  one half of the opening angle of the objective, and  $NA$  the objective's numerical aperture.

Different definitions regarding the resolution exist: i) the Rayleigh criterion, stating that two points are resolvable if the maximum intensity of the second spot is at the first minimum of the first one ( $d = res$ ; Figure 14A and B) or ii) the Sparrow criterion, defining two points as resolvable until the resulting function of the overlay of the two PSFs yields a straight line in its maximum.

For the commonly used Rayleigh criterion the resolution results in

$$res = \frac{0.61 \cdot \lambda}{NA} \quad (5)$$

and thereby in a resolution limit of about 175 nm for microscopy with visible light ( $\lambda = 400$  nm,  $NA = 1.4$ ).

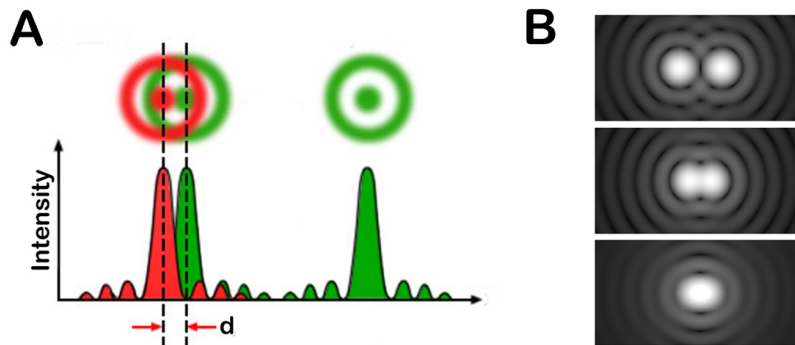


Figure 14: A) Rayleigh Criterion for Resolution Limit modified from [77]. To the right, the PSF of a single point (green) can be seen, as given by the Airy function. Left, an additional second point is shown (red). The two points are resolvable, according to the Rayleigh criterion, if the maximum of the one is at the first minimum of the other, as shown in this figure. B) Varying distances between two points and the respective ability to resolve them [70]. The upper two points are far apart and easily resolvable by eye. The middle ones are exactly meeting the Rayleigh criterion, as shown in A, whereas the two points at the bottom cannot be distinguished as two separate points any more.

### 1.3.1 Super-Resolution Methods

#### Strategies to Increase Resolution

Different approaches were used to overcome the limitation of the resolution caused by diffraction. The first ones, yet yielding only little increase in resolution, are far-field optical approaches such as  $4\pi$  microscopy, where a second objective is used to gather light of the full spherical angle, increasing the *axial* resolution to 100 nm [78].

Another method increasing the resolution is Structural Illumination Microscopy (SIM), where patterned illumination is used for sample excitation and the spatial frequencies of the illumination interact with the ones of the sample. In order to create high-resolution images, the acquisition is repeated with different phases and orientations of the excitation pattern. A spatial resolution of 100 nm was realized using SIM [79].

The two methods described do not exploit the fluorophore's physical or chemical properties. However those properties have to be taken advantage of in order to increase the resolution even more. This is realized in Stimulated-Emission-Depletion Fluorescence Microscopy (STED) by using a second laser to suppress the fluorescence emission of fluorophores outside the center of the excitation laser beam. This suppression occurs via stimulated emission, a process where the initially excited fluorophore encounters a photon bearing the exact same energy as the difference between the excited and the ground state, and is brought back to the ground state before fluorescence emission can happen.

The darkened population hereby depends on the STED laser intensity in a non-linear way, thus, the spontaneous emission can be efficiently suppressed by the stimulated emission, yielding the depletion of the fluorophore. The laser intensity, which achieves a reduction of a specific fluorophore's intensity to 50%, is called the saturation intensity, and the stimulated emission becomes the dominating process for laser intensities larger than that. By increasing the STED laser intensity, depletion is realized also in the areas close to the borders of the diffraction-limited spot, thus reducing it in size. This method was proposed in 1994 and by its realization in 2001 a spatial resolution of 65 nm was achieved ([80], [81]).

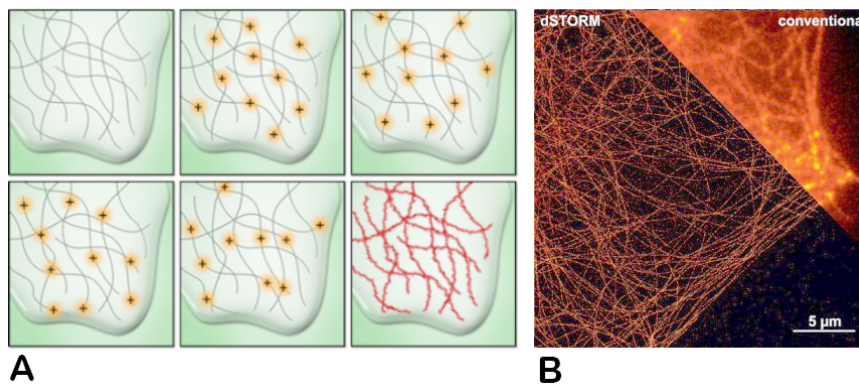


Figure 15: A) Principle of SMLM imaging [82]. Unobserved cellular structures are shown as grey tubes, whereas the observed spots are shown as black dots with yellow surroundings as their respective diffraction-limited image. After the acquisition of  $n$  images (here:  $n=4$ ), and localization of the centers of the diffraction limited spots, the integral image of the localizations is shown in the last image at the bottom right. B) Difference between super-resolution and diffraction limited microscopy [83]. At the bottom left, tube like structures can be resolved by dSTORM, whereas at the top right, a conventional diffraction-limited image of the same structure is shown.

A further group of imaging methods are stochastic ones or SMLM, which are based on the progress made in the design of fluorophores and the use of photo-activatable or switchable dyes. These can be actively switched between a dark and a fluorescent state; thereby, spatially overlapping molecules can be separated in the time domain and the resulting images can be superimposed. A sufficiently low density of activated fluorophores has to be ensured, so that single ones can be distinguished from each other in one image. The increase in resolution is caused by the localization of the single fluorophores via fitting a PSF and determining the real position with accuracies of typically up to 15 nm. This method is used e.g. in PALM [84], Stochastic Optical Reconstruction Microscopy (STORM) [85] or direct STORM (dSTORM) [86].

## Fluorophores

Only the use of specific photo-switchable fluorophores enabled PALM measurements. Heilemann et al., however, showed in their application of dSTORM, that also conventional organic fluorophores, such as Cy5 or Alexa Fluor 647, can be photo-switched, and thus, be used for SMLM ([87], [86]).

Important characteristics for all employed fluorophores in SMLM include a large extinction coefficient as well as a large quantum yield, resulting in high number of detectable photons.

One irreversibly photoactivatable fluorophore is the Eos fluorescence protein. Initially, a monomeric form of Eos (mEos) could not be formed above 30°C, limiting its use in live cell applications [88]. A further development, mEos2, could solve this limitation, while representing a not truly monomeric form [89] as shown by Zhang et al. [90], who also achieved to produce a monomeric version named mEos3.2.

Another method of realizing photo-activation is by caging of the fluorophores by certain protective groups. Irradiation with ultraviolet light can release this group, and enables activation of the fluorophore. One example for such fluorophores is the red-emitting STAR635 (abberior, Göttingen, Germany, [91]), and its caged version CAGE635 (abberior, Göttingen, Germany, [92]).

When using non-genetically encoded fluorophores, specific attention has to be given to their interaction with other parts of the experimental system, e.g. their unspecific binding to a lipid bilayer [93].

## Localization Algorithms and Uncertainty

An object's image is produced by the convolution of the object itself with the PSF. Therefore, the position of the object can be determined via de-convolving the image with the respective PSF. This is the primary principle all SMLM-Methods are based on. In practice, the PSF of an imaging system can be approximated by a Gaussian. Commonly used measures for the fitting routine are the least-squares (LS) and the maximum likelihood estimation (MLE). For LS, the differences between the predicted and the actual signal are calculated and their squares are summed. A further development, is using weighted LS (wLS), where the squares are weighted before summing. This sum is minimized in LS. MLE includes a model for noise. Combining this with a model PSF, different parameters, such as coordinates, intensity, background etc. are assumed, and the likelihood for obtaining the observed signal is calculated. MLE outperforms (w)LS in almost all cases, with (w)LS doing equally well in presence of signals with high photon

counts. However, most MLE algorithms are considerably more time consuming than LS-based ones [94].

An analytical expression for the localization uncertainty was derived by Thompson et al. It consists of the sum of two terms, representing i) a case, where the accuracy is limited by the shot noise of photons and ii) a case, where the limitation arises because of the background noise. However, they detected an error of about 30% between theoretical estimations and Monte Carlo simulations [95]. In 2010, Mortensen et al. showed that this equation violates the Cramer-Rao bound, which dictates the minimally possible accuracy, and renewed it, resolving the 30% error, by introducing the factor 16/9 and thereby revoking the permanent underestimation by the former widely used equation of Thompson yielding:

$$\langle \Delta x^2 \rangle = \frac{16}{9} \frac{s^2 + \frac{a^2}{12}}{N} + \frac{8\pi s^4 b^2}{a^2 N^2}, \quad (6)$$

with  $a$  the pixel size,  $N$  the number of detected photons,  $b$  the background photons, and  $s$  the standard deviation of the PSF [96].

### 1.3.2 Single Molecule Tracking

To gain a deeper understanding of the behaviour of proteins within the cell, also the proteins lateral movement has to be considered. Different methods to extract the quantitative measure for this diffusion, i. e. the diffusion coefficient,  $D$ , exist. This diffusion coefficient represents the particles mobility within a specific surrounding, e.g. the cellular membrane.

### Two-Dimensional Diffusion

The diffusional analysis of particles is based on their mean square displacement given by

$$\langle r^2 \rangle = 4Dt \quad (7)$$

with  $t$  being the time and  $D$  the diffusional coefficient.

This relation results from the solution of Fick's second diffusion law, derived from the Brownian motion of molecules.

However, there are situations where this random motion is not the driving one, such as directed or restricted motion. The relation then is

$$\langle r^2 \rangle \propto t^\alpha \quad (8)$$

with  $\alpha > 1$  yielding superdiffusion (e.g. directed, active cellular transport processes), and  $0 < \alpha < 1$  resulting in subdiffusion (e.g. due to intracellular crowding [97]).

## Tracking Methods and Algorithms

Different techniques can be applied to get an estimation about the lateral mobility of certain molecules within membranes. Amongst them is Fluorescent Recovery After Photobleaching (FRAP), which is based on the recovery of fluorescence in a previously photobleached area due to the diffusion of non-bleached molecules into this area. This method gives a measure of the mobility of the whole ensemble of molecules. Commonly, a two-component model is found, including one mobile (70-95%) and one immobile fraction.

Additionally, SMT methods have been developed and the reduction of the label size down to single fluorophores, made the visualization of local heterogeneities in diffusion possible [98].

For SMT the density of visible fluorophores within an image has to be restricted to a degree, where the individual fluorophores can be resolved. This can either be accomplished by a very low labelling density, as done in classical SMT measurements, or by stochastic activation of a limited number of fluorophores, as established within PALM. This new approach was termed single particle tracking PALM and enables to get the same statistics from a single cell as for SMT with up to hundred cells [99].

For the analysis of these tracks, first, the positions of the molecules in each single image have to be determined. This can be realized the same way as done within SMLM. The ensuing linkage of the molecules in consecutive frames is a challenging task, with different approaches available. 14 different algorithms were evaluated in a comprehensive overview of Chenouard et al. [100]. Most of those employ a pre-filtering before identifying the molecule's position, mostly via a preceding maxima detection with consecutive PSF fitting, as described earlier. The subsequent linking of the localizations is realized in a multitude of different ways. The most straight-forward approach is the nearest neighbour analysis. The respective localizations in consecutive frames are connected to the point with the minimum distance. This 'single-frame' approach, however, exhibits major faults, especially when fluorophores are absent in some frames, thus adding gaps to the tracks. Therefore, algorithms to allow for missing frames within the resulting tracks already increase the reliability of the whole tracking process. In the work on hand, such a Nearest Neighbour approach with additional options to include gaps within tracks was utilized as proposed in [101]. Many tracking algorithms ('multi-frame') go a step further

and include not only the consecutive frame in the tracking process, but also consider the information of a certain amount of neighbouring frames or even the whole acquisition time. Those include for example multiple hypothesis tracking, which calculates probabilities for varying tracks and chooses the most probable one [100].

The comparison by Chenouard et al., however, made clear that there is no perfectly reliable and universally applicable tracking algorithm up to now. Problems occur especially when analyzing images with low SNR and high densities. While the low SNR increases the difficulty of identifying real signals and distinguishing them from noise, the high density turns the linking of the signals into a challenging problem, as overlapping tracks will occur.

A method to overcome the issue of high densities and still determine the diffusion characteristics of a protein was developed by Schmidt et al. and is termed Particle Image Correlation Spectroscopy (PICS) [102]. Here, the linking of acquired signals is omitted, and the mobility is determined by a correlation function between an image A at time-point  $t_1$  and an image B at time-point  $t_1 + t_{lag}$ . The shifting distance hereby is varied, and for a movement of the particle in one  $t_{lag}$ , which approximates the shifting distance, the correlation function is high. As no linking of particles is applied, the overlap of possible tracks does not affect the outcome of the analysis.

## MSD Analysis

One way to determine  $D$  is via the MSD, introduced previously. The displacement distances can be extracted from each track identified in the tracking experiment. The distance between two consecutive points of each track is calculated and the mean value is drawn in a plot of the MSD over the time. The same procedure is done with gaps between the consecutive points, e.g. determining the distance between the first (or second etc.) and the third (or fourth etc.) point of each track. The  $MSD$  values for a single track can be determined using Equation 9.

$$\langle r^2 \rangle = MSD_{\Delta t=i} = \frac{1}{n-i} \sum_{t=1}^{n-i} (x_t - x_{t+i})^2, \quad (9)$$

with  $n$  being the total number of points within the track,  $i$  the size of the introduced gap and  $x$  the positions.

In this way, the time dependence of the MSD is derived. However, this is done in a discrete way as the images are recorded with a certain delay between them, called the

time lag  $t_{lag}$ . An exemplary plot of the MSD over time for free Brownian motion is shown in Figure 16C. The diffusion coefficient can be determined by fitting e.g. Equation 7 for linear diffusion. For this fitting procedure, Wieser et al. showed by using Monte Carlo simulations that the use of only the first two data-points already yields the most accurate estimation of  $D$  as the error  $\sqrt{\langle (D_{fit} - D)^2 \rangle}$  is minimal. This is due to the mutual dependency of the data-points [103]. In most of these representations of the MSD

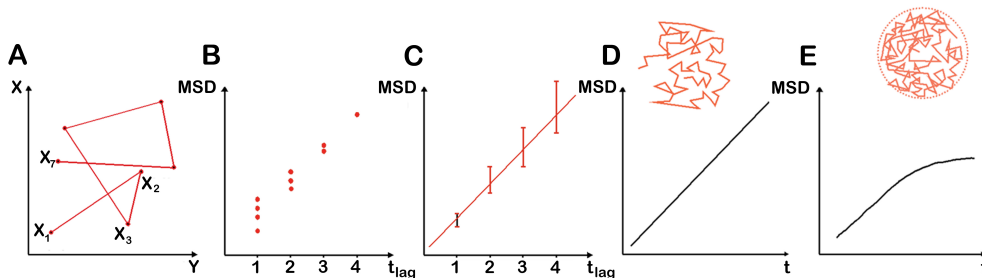


Figure 16: A) measured track, with the respective positions of the particle at different, consecutive frames ( $x_1 - x_4$ ). B) MSD information is extracted by taking consecutive positions (e.g.  $x_1-x_2$  or  $x_2-x_3$ ), and then introducing gaps of increasing size. In C) the mean values for different  $t_{lag}$  are calculated, and Equation 7 is fitted. Note the error bars getting larger for increased  $t_{lag}$ , as the number of contributing data points in B decreases. D) shows a characteristic plot of MSD over time for free Brownian motion of a particle, whereas in E) MSD drawn over time of a particle experiencing spatial restriction is shown [104].

over time, a certain offset is present, which is due to the limited positional accuracy (PA) of the localization algorithms [105], and affects the MSD as follows:

$$\langle r^2 \rangle = 4Dt + 4\sigma^2 \quad (10)$$

with  $D$  the diffusion coefficient,  $t$  the time,  $r$  the displacement and  $4\sigma^2$  the PA representing the standard spatial deviation from immobile molecules over consecutive frames. A further, qualitative measure supplied by such a MSD-analysis is the shape of the plot. Depending on the type of diffusion the particle is undergoing, the plot takes different shapes as shown in Figure 16D, E. Different analytically derived equations can be fitted, for determining  $D$  for varying types of diffusion.

## Chapter 2

# Materials & Methods

### 2.1 Cell Culture and Sample Preparation

For the retroviral transduction of primary murine T cells, Phoenix-ECO [68] cells were cultured in Dulbecco's Modified Eagle Medium (DMEM, Sigma-Aldrich, St. Louis, USA) containing 10% Fetal Bovine/Calf Serum (FBS, FCS, Sigma-Aldrich, St. Louis, USA), Penicillin, Streptomycin (Lonza, Basel, Switzerland) and L-Glutathione (Sigma-Aldrich, St. Louis, USA) and incubated at 37°C with 5% CO<sub>2</sub>. The cells were split in a way that ensured their confluence of 70-80% for optimal transfection. A stably transfected line of Phoenix-ECO- $\zeta$ -mEos was cultured with additional 50  $\mu$ g/ml Blasticidine (InvivoGen, San Diego, USA) and used for transduction. Stably transfected Jurkat- $\zeta$ -mEos cells were cultured in RPMI-1640 (Sigma-Aldrich, St. Louis, USA) with additional 10  $\mu$ g/ml Blasticidine.

T cells were isolated from murine spleen and blasts were prepared by the group of Stockinger and Huppa at the Medical University of Vienna (MUW). They were collected from the MUW and cultured in sterile filtered T Cell Medium (TCM) containing 50 ml FCS, 5 ml Non-Essential Amino Acids (Lonza, Basel, Switzerland), 5 ml Penicillin/Streptomycin, 10 ml L-Glutathione, 500 ml RPMI-1640 (Lonza, Basel, Switzerland), 5 ml Sodium Pyruvate (Sigma-Aldrich, St. Louis, USA) and 50  $\mu$ M Mercaptoethanol (AppliChem, Gatersleben, Germany).

### 2.1.1 Transformation and Plasmid Preparation

#### Transformation of *E. coli* and Midi Preparation

The  $\zeta$ -mEos plasmid was provided by Florian Baumgart. Competent bacteria were used for plasmid replication. A batch of frozen *Escherichia coli* was thawed and diluted with 20  $\mu\text{l}$  KCM buffer (KCl - CaCl<sub>2</sub> - MgCl<sub>2</sub>), 9  $\mu\text{l}$  dH<sub>2</sub>O and 1  $\mu\text{l}$  of the  $\zeta$ -mEos plasmid. The mixture was incubated for 10 minutes on ice followed by 10 minutes on room temperature. 1 ml lysogeny broth (LB) medium was added, followed by an incubation for one hour on a Thermomixer Comfort (Eppendorf, Hamburg, Germany) at 37°C and 400 rpm. 100  $\mu\text{l}$  was spread on an ampicillin coated 10 cm petri dish and incubated overnight. One culture was picked from the petri dish and incubated on the Thermomixer at 37°C with 400 rpm within 1 ml of LB medium. Approximately 8 hours later, another 50 ml of medium was added and left on the Thermomixer overnight. On the next day, the GeneJET Plasmid Midiprep Kit (Thermo Fisher Scientific, Waltham, USA) was used according to protocol for plasmid purification. The plasmid concentration was measured using a Synergy H1 Multi-Reader (BioTek, Winooski, USA).

#### 2.1.2 T-Cell Transduction

For the transduction of primary murine T cells, the protocol described in [106] was adapted:

On *Day 0*, the Phoenix-ECO (wt and/or  $\zeta$ -mEos transfected) cells were seeded in a 10 cm petri dish to reach 70-80% confluence the following day and the T cells were isolated. On *Day 1*, the Phoenix-ECO cells were double-transfected with pIB2- $\zeta$ -mEos and pIEco using the TurboFect Transfection Reagent (Thermo Fisher Scientific, Waltham, USA) and Opti-MEM medium (Life Technologies, Carlsbad, USA). Approximately eight hours later, the medium was exchanged to 5 ml of full supplemented DMEM.

On *Day 3*, the viral supernatant from the Phoenix-ECO cells was collected and spun down in order to remove cell debris. Simultaneously, 4 million T cells were spun down (1000 rpm, room temperature, full brake, 3 minutes) and resuspended in 4 ml of the virus-containing supernatant. 10  $\mu\text{g}/\text{ml}$  Polybrene (Sigma-Aldrich, St. Louis, USA) and 9  $\mu\text{g}/\text{ml}$  IL-2 (eBioscience, San Diego, USA; 50 U/ml) was added. One million cells were seeded per well on a 24-well plate. Parafilm was used to seal the plate and centrifugation for 90 minutes in a pre-warmed (32°C) centrifuge with the centrifugal brake set to zero was performed. Another 1 ml of TCM and 9  $\mu\text{g}/\text{ml}$  IL-2 were added.

On the next day (*Day 4*), the cells were split 1:2 and 15  $\mu\text{l}$  Blasticidine was added (50

$\mu\text{g/ml}$ ). Dead cells were removed by density gradient centrifugation using Histopaque 1119 (Sigma-Aldrich, St. Louis, USA) and the living cells were resuspended in TCM with  $9 \mu\text{g/ml}$  IL-2 on *Day 6*. 1 ml TCM was added daily until the experiments were performed not later than on the afternoon of *Day 9*.

### 2.1.3 Sample Preparation

#### Lipid Bilayer Preparation

The interactions of T lymphocytes with the APCs represent a challenging experimental system for 2D microscopy. By imitating the membrane of APCs with flat lipid bilayers, the third dimension can be largely excluded.

Piranha solution was used to clean the glass slide and remove any organic residues. 35 ml of  $\text{H}_2\text{SO}_4$  (Sigma-Aldrich, St. Louis, USA) was mixed with 15 ml of  $\text{H}_2\text{O}_2$  (Sigma-Aldrich, St. Louis, USA), and #1.5 glass slides (Menzel, Jena, Germany) were incubated therein for at least 30 minutes. Afterwards, they were rinsed with at least 250 ml of  $\text{dH}_2\text{O}$  and left to dry at air for ten minutes. Alternatively, they were dried with nitrogen immediately after rinsing.

For all experiments, Nunc<sup>TM</sup> Lab-TEK<sup>TM</sup> Chambers (Thermo Fisher Scientific, San Diego, USA) were used. They were kept in Ethanol (Sigma-Aldrich, St. Louis, USA) and rinsed with  $\text{dH}_2\text{O}$  before use. The piranha-cleaned glass slides were glued to the chambers by a two component dental glue.

A vesicle stock solution containing 90% 1-Palmitoyl-2-oleoylphosphatidylcholine (POPC) and 10% Nickel chelated 1,2-dioleoyl-sn-glycero-3-[(N-(5-amino-1-carboxypentyl) iminodiacetic acid)succinyl] (DOGS) was diluted 1:10 with Phosphate Buffered Saline (PBS, Lonza, Basel, Switzerland) and each well was incubated with  $150 \mu\text{l}$  for 10 minutes. After the wells were rinsed with 15 ml PBS,  $330 \mu\text{l}$  were removed from each well leading to a remaining volume of  $350 \mu\text{l}$  per well.

The wells were incubated with additional  $50 \mu\text{l}$  of PBS, containing  $0.08 \mu\text{l}$  and  $0.04 \mu\text{l}$  of his-tagged murine or human ICAM and B7-1, respectively, for 75 minutes. For experiments with activating lipid bilayers up to  $0.1 \mu\text{l}$  of the respective pMHC (unlabelled, -A647, -A555) was added. Afterwards, the wells were rinsed with 15 ml PBS two times. To check the transduction efficiency, slides were coated with  $50 \mu\text{g/ml}$  Fibronectin (FN; Sigma-Aldrich, St. Louis, USA) by incubation of PBS-diluted FN for at least 30 minutes.

## T-Cell Preparation, Labelling and Sample Completion

For all performed T cell experiments, one million cells were suspended in 2 ml TCM and spun down in FACS tubes, the supernatant was discarded, and the cells were washed once with 2 ml Hank's Balanced Salt Solution (HBSS, Lonza, Basel, Switzerland) containing 2% FBS (imaging buffer).

Differently labelled scFv's were used for both, tracking and (two-color) PALM experiments. After the last washing step, approximately 50  $\mu$ l of cell suspension remained in the FACS tube. 0.2 - 2  $\mu$ l of the respective scFv was added, followed by incubation on ice for 10 to 15 minutes. The cells were washed at least once with cold imaging buffer. While the scFv-STAR635 labelling was finished at this point, an incubation with 2  $\mu$ l Streptavidin-labelled Abberior CAGE635 for 10 to 15 minutes on ice was done for the biotinylated scFv. The cells were washed two times with cold imaging buffer and kept on ice. All the washing steps were done using a pre-cooled centrifuge (4°C).

1 to 10  $\mu$ l of the resulting T cell suspension was injected into the corner of the wells of LabTEK chambers. Before that, the buffer in the well was exchanged with imaging buffer by adding and removing 250  $\mu$ l imaging buffer up to 10 times.

For experiments with fixed cells, labelled cells were resuspended in 30 to 50  $\mu$ l imaging buffer and the whole volume was added to one well and incubated for 10 to 25 minutes. For PALM experiments on activating bilayers, the cells were incubated 20 minutes before fixation. 250  $\mu$ l Paraformaldehyde (PFA; 8%, room temperature) was gently added and removed twice - followed by an incubation of 10 to 15 minutes at room temperature. The buffer was exchanged to PBS. The PFA concentration as well as the incubation time were adjusted following a protocol by Whelan et al. [107].

For calcium flux measurements, Fura2-AM (Life Technologies, Carlsbad, USA) was used. One million T cells were washed and incubated for at least 15 minutes at room temperature on a Thermomixer Comfort at 400 rpm with Fura2-AM, diluted 1:200 in 200  $\mu$ l imaging buffer. The cells were washed two times with imaging buffer and resuspended in 150  $\mu$ l of imaging buffer. 20  $\mu$ l were added to one well of a LabTEK chamber containing the respective surface.

## 2.2 Laser, Microscopes and Cameras

Experiments were performed on two different microscope setups, referred to as SDT1 and SDT3.

### 2.2.1 SDT 1

All tracking and PALM experiments were performed on SDT1. For the photo-switching/uncaging of mEos/CAGE635, a 405 nm diode laser (iBeam smart, Toptica, Grafelfingen, Germany) was used. Images were acquired by excitation with a green laser at 532 nm (Millennia X, Spectra Physics, Santa Clara, USA) and a red Krypton ion laser at 647 nm (Innova 300, Coherent, Santa Clara, USA) respectively. All laser lines passed acousto-optical modulators (AOMs; Isomet, Springfield, USA) and were coupled into an inverted light microscope - a Zeiss Axiovert 200 (Zeiss, Jena, Germany) - via multiple mirrors.

An oil-immersion  $\alpha$ -plan Aplanachromat (Zeiss, Jena, Germany) objective with a NA of 1.46 was used. This objective enabled the use of objective-based TIRF as described before. Since the same objective was used for excitation and detection, a quad band TIRF filter (ZT405/488/532/640rpc, Chroma, Bellows Falls, USA) was used.

Two color measurements were performed using the DV2 Multichannel Imaging System (Tucson, USA), with the corresponding filters (HQ585/40m and HQ700/75m, Chroma) inserted, to split the emission light. The light was collected by an Andor iXon Ultra EMCCD camera (Belfast, UK) cooled down to  $-60^{\circ}\text{C}$  for reduction of thermal noise.

An in-house programmed LabVIEW (National Instruments, Austin, USA) package was used to control the laser shutter, the AOM, the EMCCD camera and the TIRF illumination.

### 2.2.2 SDT 3

Calcium flux experiments were performed on the setup SDT3. The Fura2-AM loaded T cells were excited using a monochromatic light source, the Polychrome V (TILL Photonics - FEI Munich, Grafelfing, Germany). The light was coupled to a Zeiss Axiovert 200M microscope via a TILL System consisting of a Polytrope/Yanus combination by TILL Photonics. Two different objectives were used: first, the UPlanFN 10x air objective (Olympus, Tokyo, Japan) was used to acquire images containing a high number of cells for statistical analysis, and second, the UPlan FLN 40x (Olympus, Tokyo, Japan) was used to get more detailed information on the  $\text{Ca}^{2+}$ -flux. The image was recorded by an Andor iXon Ultra. For image acquisition and light source controlling, Live Acquisition 5 (TILL Photonics - FEI Munich, Grafelfing, Germany) was utilized.

## 2.3 Image Recording

Varying image recording sequences were used for the different experiments. They were adapted to the needs of the experiment as well as to the used fluorophores and their bleaching behaviour.

### (Two-Color) PALM Image Recording

For (two color) PALM experiments, sequences with illumination times of 2 to 3 ms and a time delay of 5 to 10 ms between the images were used. In case of two color experiments, both the image acquisition of two colors and the activation/uncaging of mEos/CAGE635 was done simultaneously. 1000 to 5000 frames were recorded. The illumination power for the red, green and ultraviolet (UV) lasers were 1.2 - 1.7, 0.6 - 1.5 and 0.02 - 0.6 kW/cm<sup>2</sup>, respectively.

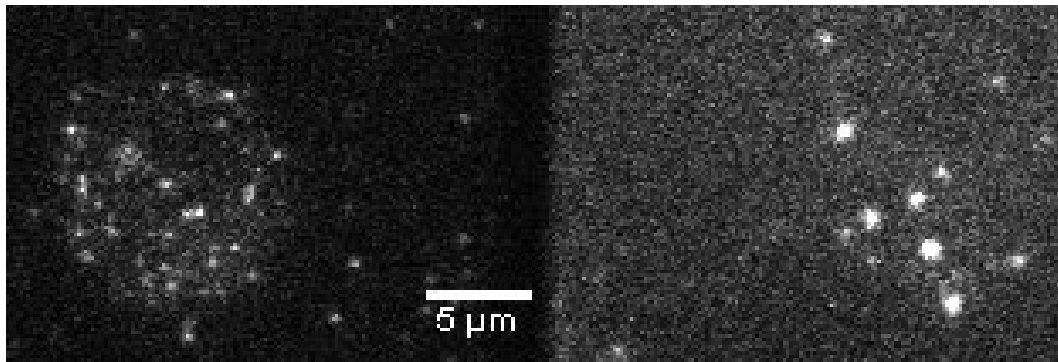


Figure 17: One frame of two-color PALM image of  $\zeta$ -mEos transfected primary murine T cell. Left) the photoactivated  $\zeta$ -mEos, right) the uncaged TCR $\beta$  with scFv-CAGE635.

### Simultaneous SMT and PALM

For experiments with combined SMT and PALM measurements, an illumination protocol was designed as shown in Figure 18. The laser power for the recording of PALM images was carefully adapted within the previously given range to yield a trade-off between the desired bleaching of mEos within PALM, and extensive undesired bleaching of STAR635 for SMT. The tracking images were recorded using a laser power of 0.65 - 0.8 kW/cm<sup>2</sup>.

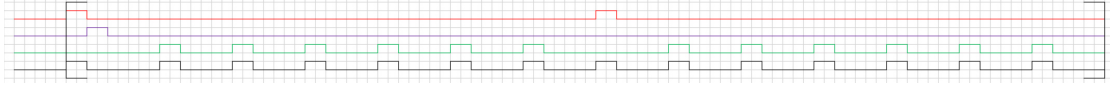


Figure 18: The imaging sequence for simultaneous PALM/SMT image recording. One square equals 1 ms, and the colors represent the excitation lasers of the respective colors. The black line shows the camera trigger. The bracketed sequence was repeated up to 512 times, resulting in 7168 recorded images, where SMT (red) to PALM (green) images were recorded in a ratio of 1:6.

## Calcium Flux Measurements

Alternating images were taken with excitation wavelengths of 340 and 380 nm and respective illumination times of 50 and 10 ms. Delay times of 54 and 45 ms resulted in a total cycle time of 159 ms. This sequence was repeated between 500 to 1000 times, with a delay of 841 ms between individual image duplets.

## 2.4 Image Analysis

### 2.4.1 Calcium Flux Analysis

For qualitative analysis of  $\text{Ca}^{2+}$  flux experiments, the ratio images were calculated using a self-written ImageJ (National Institute of Health, Bethesda, USA) macro based on the *Ratio Plus* plugin (Magalhaes, P., University of Padua, Italy).

A self-written MATLAB (MathWorks, Natwick, USA) program was used to obtain quantitative intensity tracks. The ratio image was calculated, an intensity threshold was applied and its contrast was enhanced using a Wiener filter. This filter utilizes an estimate of the global noise variance ( $v^2$ ) of the image, the local mean  $\mu$  and the local variance  $\sigma^2$  within a certain range of the pixel to apply an adaptive low-pass filter of the image, according to

$$\hat{I}(x, y) = \mu + \frac{\sigma^2 - v^2}{\sigma^2} (I(x, y) - \mu).$$

Generally, two scenarios can occur:

1.  $\sigma^2 \approx v^2$ : The resulting pixel value will assume the average value  $\mu$ , or
2.  $\sigma^2 > v^2$ : The resulting pixel value will be changed only slightly.

Using this filter, flat regions within the image are blurred, whereas edges – characterized by a large local variance  $\sigma^2$  - are kept.

Circular features were extracted using a Hough transform. This transformation facilitates extraction of any geometrical shapes, which can be parameterized, such as lines or circles.

Each non-zero pixel of the initial image is transformed and represented by combinations of parameters ( $x$ ,  $y$  and  $r$  for a circular transform) which could give rise to this pixel. This analysis results in a three-dimensional parameter space, where the first two dimensions correspond to the original image, hence, the maximal pixel values in this transformed  $x$ - $y$  plane represent the centers of the circles. In order to reduce computational cost, it is recommended to use restrictions for the possible radii of the circles, thus limiting the third dimension of this transformation. Figure 19 depicts an exemplary detection of a circle within the  $x$ - $y$  plane.

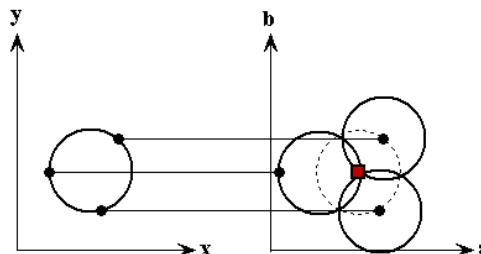


Figure 19: Exemplary representation of the circular Hough transform for a fixed radius. Three non-zero pixel are represented and transformed, yielding the center of the circle in the transformed  $a$ - $b$  plane, corresponding to the position of the center in the original  $x$ - $y$  plane [108].

The corresponding features were linked over all recorded images. The features' total intensity was determined and normalized to its area. An intensity-threshold was extracted from the positive control in order to assess the ratio of cells undergoing  $\text{Ca}^{2+}$  flux.

## 2.4.2 Single Molecule Localisation

In order to separate the two color channels as well as the respective tracking or PALM images, the raw images were pre-processed by self-written ImageJ macros.

The images were fitted by the ImageJ plugin thunderSTORM [109]. First, a pre-filtering in form of a wavelet (B-Spline) filter of order 3 and scale 2 was applied. The localizations were approximated by finding local maxima with a threshold of 1.5 times the standard deviation of the first wavelet level, which was determined in the pre-filtering step in a 8-neighbourhood. The sub-pixel localization was performed by fitting an integrated gaussian as PSF using MLE with a radius of 6 pixel and an initial sigma of 1.6 pixel. For information on the used algorithms refer to [110].

The positional accuracy was calculated according to an equation, which accounts for the characteristics of an EMCCD camera, proposed by Quan et al. ([111], [112]). This

equation still underestimates the PA, however, to a lesser extent than the equation proposed by Thompson et al., described previously.

### 2.4.3 Tracking and Displacement Analysis

The positions of the fitted molecules were filtered for intensity, Full Width at Half Maximum, PA and, in case of live cell PALM, a Region of Interest (ROI) by using thunderSTORM. The ROI was chosen in a way to exclude the borders of the cell, where three dimensional diffusion interferes with the observed 2D diffusion at the interface between the cell and the bilayer.

The localisations were imported in MATLAB and reformatted to fit the needs of the further analysis software, *particle\_tracking\_2D* - an in-house implementation [113] of an algorithm designed by Gao et al. [101]. The parameters used within this software are: i) the maximum distance of molecules to link in consecutive frames ( $d_{max}$ ), ii) the minimum length of tracks ( $l_{min}$ ) and iii) maximum number of frames a molecule can be missing ( $fr_{omit}$ ). Those parameters were adjusted to the fluorophores and the method of acquisition, i.e. PALM or SMT. The particular values can be found in Table 1.

Label	$d_{max}$ [px]	$l_{min}$ [#]	$fr_{omit}$ [#]
mEos3.2	2	2	1
CAGE635	2	2	1
STAR635	3	5	0

Table 1: Parameters used for the tracking algorithm and the respective fluorophores.

The resulting tracks of each single cell were analyzed using the in-house software *msdplot*, which yields plots of the MSD over time as well as an estimation of their diffusional constant. Cells were selected based on the calculated PA, the standard deviation of  $D$  and  $D$  itself. The tracks of all selected cells were then combined and analysed using *msdplot*, applying additional thresholds for the track length. Furthermore, a bi-exponential equation was fit to the cumulative density function (CDF) of the square displacements by the in-house program *explot*, as described in [98], to

$$CDF = 1 - \alpha \cdot e^{-\frac{x^2}{MSD_1}} - (1 - \alpha) \cdot e^{-\frac{x^2}{MSD_2}}.$$

#### 2.4.4 Evaluation of Tracking Algorithm

For the evaluation of the utilized localization and tracking algorithms, a simulated dataset provided by Chenouard et al. [100] was used. The group used this dataset for a comprehensive and objective comparison of different algorithms. The provided images were analyzed by either the previously described thunderSTORM routine, or the integrated algorithm of the used tracking software *particle\_tracking\_2D*. The subsequent tracking was in both cases performed using *particle\_tracking\_2D*. The resulting tracks were reformatted to fit the file format necessary for automated evaluation with an Icy (Quantitative Image Analysis Unit, Institut Pasteur, Paris, France) plugin provided by Chenouard et al [100].

In their work, they furthermore presented a way to determine the performance of tracking algorithms, by comparing the results to a provided ground truth. First, the distance between tracks from the ground truth ( $X = \{\Theta_k^X, k = 1, \dots, |X|\}$ , with the tracks  $\Theta$ ) and the determined tracks (Y) was calculated. This was done by computing the gated Euclidean distance for each pair of tracks and matching the pairs with minimal distance:

$$d(\Theta_1, \Theta_2) = \sum_{t=0}^{T-1} \left( \|\Theta_1(t) - \Theta_2(t)\|_{2,\epsilon} \right)$$

with the total frame number  $T$ , and the tracks  $\Theta_1$  and  $\Theta_2$ . The gating was introduced to penalize tracks further apart than  $\epsilon = 5$  pixels.

For comparing whole sets of tracks, Y was extended with  $|X|$  empty dummy tracks resulting in the set  $\tilde{Y}$ . The tracks within  $\tilde{Y}$  were assigned to tracks from the ground truth according to their minimal distance.  $\Omega$  describes the possible assigned sets resulting from matching  $\tilde{Y}$  to X. The distance between two matched track sets is defined as:

$$d(X, Y) = \min_{Z \in \Omega} \sum_{k=1}^{|X|} d(\Theta_k^X, \Theta_k^Y).$$

The task now is to find a set  $Z^* \in \Omega$  by rematching  $\tilde{Y}$  and taking a subset with  $|X|$  tracks, that minimizes the distance between  $Z^*$  and X. Afterwards, five measures were introduced to quantitatively describe the performance of the algorithms. Briefly, those are:

1.  $\alpha = 1 - \frac{d(X,Y)}{d(X,\emptyset)}$

With  $d(X,Y)$  describing the minimal distance between the ground truth (X) and the estimated tracks (Y).  $d(X,\emptyset)$  is the distance between the ground truth (X) and

a dummy set of tracks, thus describing the maximum possible distance.  $\alpha$  ignores the tracks in  $Y$  which did not get into the final set of tracks  $Z^*$  and ranges between 0 and 1.

$$2. \beta = \frac{d(X, \emptyset) - d(X, Y)}{d(X, \emptyset) + d(\tilde{Y}, \emptyset)}$$

$d(\tilde{Y}, \emptyset)$  represents the distance between the estimated tracks which did not get into the final set of tracks  $Z^*$  ( $\tilde{Y}$ ) and a dummy set of tracks. An additional penalty for unpaired tracks is therefore introduced.  $\beta$  ranges from 0 to  $\alpha$ .

$$3. JSC = \frac{TP}{TP + FN + FP}$$

As the above mentioned performance values ( $\alpha$  and  $\beta$ ) are prone to errors in localization as well as association errors, a measure to characterize only the localization was introduced. JSC describes the Jaccard similarity coefficient based on the localizations. Here, TP describes the True Positive localizations, defined as points within paired tracks, with a distance smaller than  $\epsilon$ . The False Negatives (FN) are the localizations from the ground truth ( $X$ ) which are paired with dummy positions in  $Z^*$ , and False Positives (FP) are the positions in  $\tilde{Y}$  and the non-matched ones in  $Z^*$ . JSC ranges from 0 to 1.

$$4. JSC_t = \frac{TP}{TP + FN + FP}$$

$JSC_t$  describes the Jaccard similarity coefficient for whole tracks. Here, the True Positives (TP) are defined as the non-dummy tracks within  $Z^*$ . False Negatives (FN) comprise the dummy tracks within  $Z^*$  and the False Positives (FP) are the tracks in  $\tilde{Y}$ .  $JSC_t$  again ranges from 0 to 1.

#### 5. *RMSE*

Finally, the random mean square error of the True Positive localizations considered within JSC was calculated and chosen to be a representative measure for the accuracy of positional fitting.

### 2.4.5 Cluster Analysis

The localizations were filtered for cluster analysis as described before. However, due to possible multiple detections of the same molecule, either by photo-blinking or activation over multiple images, a merging algorithm provided by thunderSTORM was applied with the following parameters: i) the maximum distance between two localizations in consecutive frames ( $d_{max}$ ) and ii) the maximum number of frames in which the localization can be absent ( $t_{dark}$ ). During PALM image analysis, however, the complexity of quantitative PALM imaging was noticed and modified thresholds used by different groups, such

as [51] and [55], were examined. Furthermore, the influences of over-counting and the power of this merging to overcome this issue, were investigated in regard to the results of Ripley’s K cluster analysis. For a first analysis, a value in the order of the median of the positional accuracy was chosen for  $d_{max}$ , typically between 25 and 50 nm. The number of off-frames was set to 50 frames corresponding to  $\approx 0.5$  s, as the off-time for mEos2 was determined to be 0.4 s ([114], [115]). However, the utilized mEos3.2 might possess different photo-characteristics, and also the used illumination protocol differs. The values used for this first analysis resemble the ones used by Lillemeier et al. and Roh et al.: low values for  $d_{max}$  (half the pixel size; 80 nm) and low values of  $t_{dark}$  (zero), corresponding to merging of molecules exclusively found in consecutive frames ([51], [58]), thereby ignoring possible photo-blinking.

Additionally, the resulting images were investigated by plotting the localizations color-coded as function of the frame number. The x-coordinates of localizations were depicted over the frame number [116]. As the parameters used for the merging algorithm are crucial for any further quantitative analysis, the cluster analysis was repeated using increased values for  $t_{dark}$  (2 s) and  $d_{max}$  (100 nm).

To determine suitable parameters for merging, a method proposed by Annibale et al. was used [115]. Here, the dependence of the number of localizations on the different dark-times is used to extract the number of actual molecules in the image, as well as the amount and characteristics of the fluorophores photo-blinking. A semi-empirical equation is fit to this curve to extract these values. Rossy et al. extended this model to take different time-scales of blinking into account. Data were fit to the following model [55]:

$$N(t_d) = N \left( 1 + n_{blink1} \cdot e^{\frac{1-t_d}{t_{off1}}} + n_{blink2} \cdot e^{\frac{1-t_d}{t_{off2}}} \right), \quad (11)$$

with  $N(t_d)$  representing the number of localisation,  $N$  the number of present fluorophores in the image,  $n_{blink1}$  and  $n_{blink2}$  the extent of blinking and  $t_{off1}$  and  $t_{off2}$  the respective off-times of the fluorophores.

Subsequently, Ripley’s K function was used to quantitatively examine the degree of clustering.

## Ripley’s K Function

The localizations were exported from thunderSTORM and imported in MATLAB, reformatted and analyzed by the in-house program *mRipleyK*.

This program uses the Ripley's K function to distinguish between random distributions and clustering of points, given by:

$$K(r) = \frac{E(r)}{\lambda},$$

with  $E(r)$ , the number of localisations within a distance  $r$  of another localisation, and  $\lambda$  the density of localisations. As the number of localizations within a certain radius is higher for a clustered distribution of points than for random distributions,  $K(r)$  can be used to determine clustering [117]. The distance, where the normalized K-function  $L(r) - r = \sqrt{K(r)/\pi} - r$  reaches a maximum, represents the radius of a circle around each point, wherein the maximum number of other localizations per area are present.

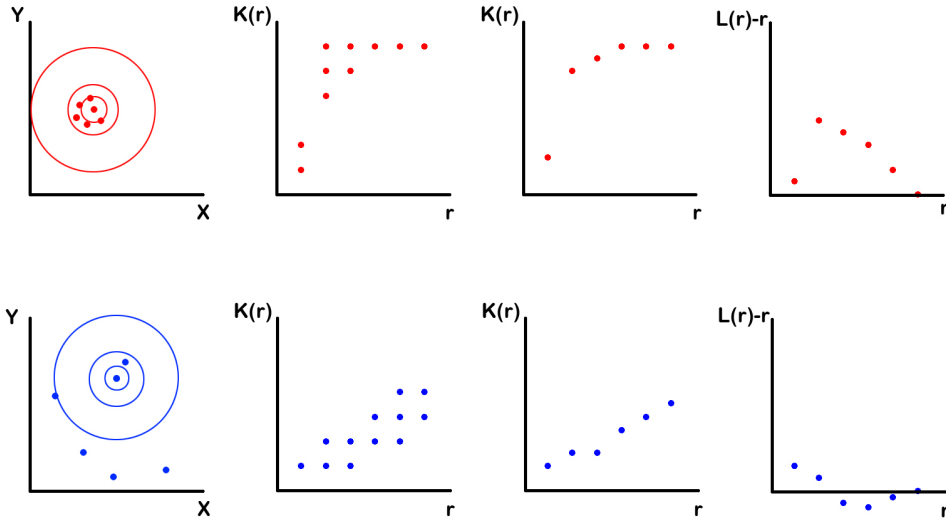


Figure 20: Ripley's K analysis for spatially clustered signals (red, top panel) and randomly distributed signals (blue, bottom panel) with  $n = 6$ . The first graph shows the raw signals with three circles of different radius around one selected signal. The second graph indicates the different values of  $K(r)$  derived from all 6 data points. Multiple values of  $K(r)$  are not indicated. The third graph shows the mean  $K(r)$  values from all six data points and the fourth graph shows an exemplary  $L(r)-r$  graph for the red and blue signal. Clustering of the red signals up to a radius of  $2r$  can be seen, whereas the  $L(r)-r$  values for the blue signal do not vary significantly from zero.

However, this value is often interpreted as the radius of apparent clusters, but the quantitative information obtained by this analysis has to be considered delicately and other ways to extract the cluster size have been proposed, e.g. taking the first derivation of  $L(r)-r$  was presented to eliminate cumulative effects [118]. Nevertheless, this maximal

value was shown to approximate the size of apparent clusters and to overestimate the size by a maximum of two-fold [118]. The maximal value of  $L(r)-r$  can be interpreted as the degree of manifestation of clusters, or how pronounced they are. The higher this value, the less localizations may be found between detectable clusters, and/or the denser are the clusters.

# Chapter 3

## Results

### 3.1 Transduction of Primary Murine T Cells

Primary murine T cells were infected with  $\zeta$ -mEos based on the protocol of Zhong et al. [106]. Due to ineffective transductions during the first attempts, the protocol was adjusted and the retroviral transduction of  $\zeta$ -mEos could subsequently be accomplished (see Section 2.1.2.T Cell Transduction for details). Several possibilities were tested to increase the transduction efficiency: The use of stably transfected Phoenix- $\zeta$ -mEos for virus production, as well as the use of medium without Penicillin/Streptomycin for transfection of Phoenix-ECO cells showed no effect. A second spin infection with repeated addition of viral supernatant to the murine T cells did not yield an increase in transduction efficiency. The addition of IL-2 during the spin infection as well as deceleration with the centrifugal brake set to zero led to better results of the transduction.

### 3.2 Calcium Flux

In order to test the potency of the available T cells as well as of the infected  $\zeta$ -mEos T cells,  $\text{Ca}^{2+}$  flux experiments were performed. Different surfaces were checked for their capability to initiate  $\text{Ca}^{2+}$  flux. A MATLAB program was written to extract the percentage of cells undergoing  $\text{Ca}^{2+}$  flux as well as their ratio tracks over time. Figure 21 shows the GUI of this software with two exemplary ratio tracks.

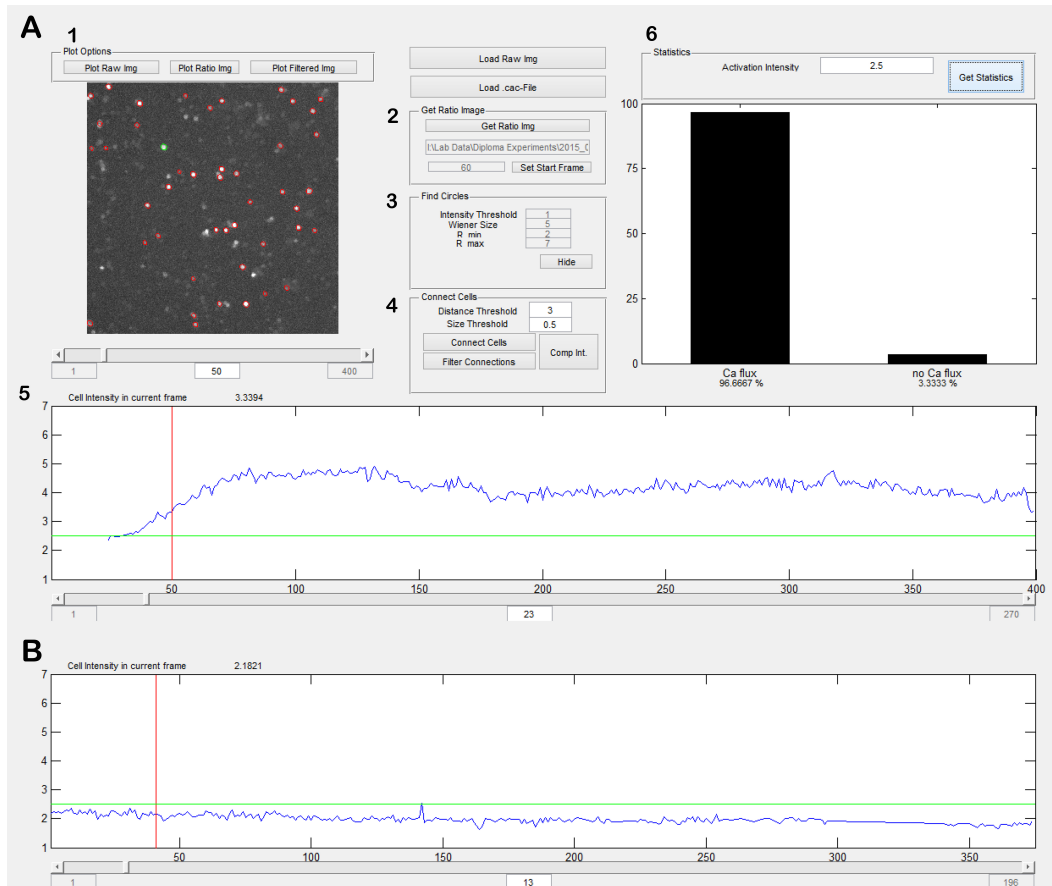


Figure 21: A) GUI for  $\text{Ca}^{2+}$  flux analysis. The following panels can be seen: 1) 'Plot Options': Three Images can be shown below this panel, which are i) the raw image, ii) the calculated ratio image and iii) the processed image after contrast enhancement using a Wiener filter. Below the image, a slider as well as frame indicators are added to navigate within the time stack. 2) 'Get Ratio Image': After loading a raw image, the ratio image is calculated by pressing this button. A starting frame can be set and used for this calculation. 3) 'Find Circles': In this panel, the threshold for the ratio image, the size of the neighbourhood used for the adaptive Wiener filter (e.g. 5 pixels) as well as the radius limitation (e.g. 2 – 7 pixel) for the Hough transform can be set. Using the button *Hide*, the red and green indicators of the identified circular cells can be turned off and on. 4) 'Connect Cells': A distance and a size threshold can be chosen for connecting cells in consecutive frames. Cells further away than the set distance threshold will not be linked, neither will be cells with a size differing more than the size threshold. Via 'Filter Connections', only tracks with more than 50 localizations are kept, and by 'Comp Int.' the normalized integral intensity is calculated. 5) 'Plot of ratio tracks': A specific ratio track (shown in blue) can be selected in the bottom of the plot by inserting the track number. The red line indicates the actual frame shown in the image above, with the respective ratio value shown in the plot title. The slider below allows to switch through all cells identified, while highlighting the current cell in green within the image. The green line indicates the 'Activation Threshold', specified in 6) 'the statistics panel'. The percentage of cells undergoing  $\text{Ca}^{2+}$  flux is calculated by defining cells with ratio values above the threshold for at least 35 consecutive frames as cells with  $\text{Ca}^{2+}$  flux positive, and the rest as no  $\text{Ca}^{2+}$  flux (negative). B) respective ratio track of a cell not undergoing  $\text{Ca}^{2+}$ .

The threshold to determine the calcium flux was manually selected by choosing up to five cells with observable  $\text{Ca}^{2+}$  flux within the ratio image of the positive control. For these cells, the ratio intensity before and after  $\text{Ca}^{2+}$  flux initiation were extracted, and the average value of the two extrema was calculated. Then, the mean value of the five analyzed cells was calculated and used as threshold. Figure 22A shows the results for the respective surfaces. The potential for inducing calcium flux of the further used pMHCs, including two labelled forms (A647, A555) was confirmed.

Untreated glass slides, fibronectin-coated surfaces, and ICAM/B7 bilayers showed only few cells with increased intracellular calcium concentrations. The experiments confirmed the potency of primary murine T cells. The potency of  $\zeta$ -mEos infected T cells was tested in a separated experiment, which confirmed their ability to initiate  $\text{Ca}^{2+}$  flux (n=9, 89%, see Figure 22B).

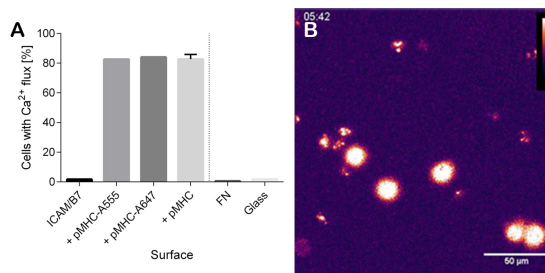


Figure 22: A) percentage of cells within a certain ROI undergoing  $\text{Ca}^{2+}$  flux on various surfaces.

Non-activating (left bar) and activating lipid bilayers were used by introducing various pMHCs species, as well as surfaces without bilayer were tested. Bars from left to right show non-activating lipid bilayers (ICAM/B7), and activating bilayers including labelled (A555, A647) and unlabelled pMHCs. Furthermore, FN and the glass slide itself were tested. B) ratio image for  $\zeta$ -mEos infected T cells, depicting five bright cells with increased intracellular  $\text{Ca}^{2+}$  levels, and one cell to the lower left, which still has normal levels.

### 3.3 Diffusion Analysis

#### 3.3.1 Evaluation and Comparison of Tracking Algorithms

The used localization and tracking algorithms were evaluated as described before and compared to the results of a total of 12 others. While the localization algorithms *per se* were performing equally for all SNR and densities (JSC, median rank: 10 for both), the localizations determined by *thunderSTORM* constitute a more reliable source for the consecutive tracking than those determined by *particle\_tracking\_2D* (JSC<sub>t</sub>, median rank: 7 and 11, respectively). This is especially the case for the scenarios with higher SNRs (4 and 7) and higher densities (mid and high). The tracking algorithm based on *particle\_tracking\_2D* localizations could not reach a top ten median rank for any of the various scenarios, whereas the same tracking algorithm, based on *thunderSTORM*

localizations showed good performance for low SNR and mid densities (median ranks: 9 and 8, respectively). Due to the results of this evaluation, *thunderSTORM* was used to localize the single molecule signals within the images, and *particle\_tracking\_2D* was used consecutively in order to connect these localizations.

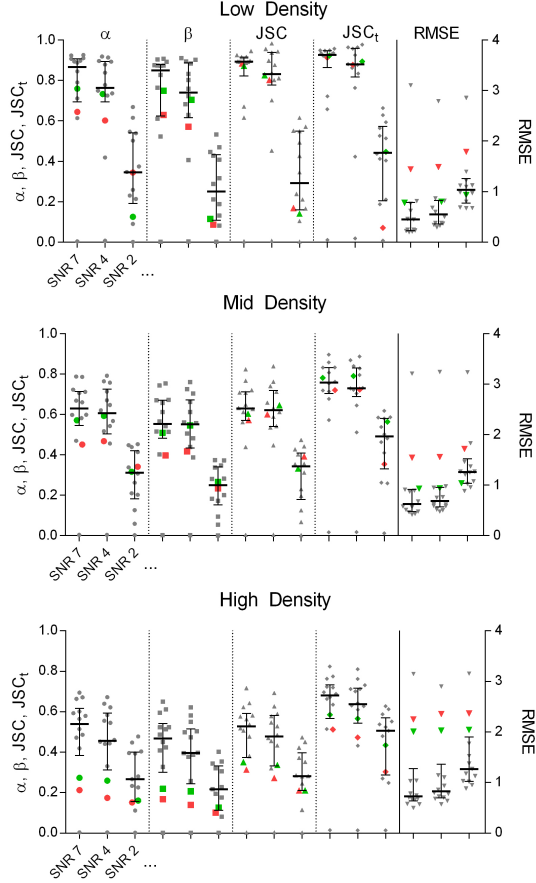


Figure 23: Two different localization algorithms (green: *thunderSTORM*; red: *particle\_tracking\_2D*) were evaluated with consecutive tracking using the same algorithm (*particle\_tracking\_2D*) in both cases. The performance was evaluated using a total of nine different scenarios provided by Chenouard et al. [100] differing in the SNR (2, 4, 7) and the density (Low, Mid, High). The data of 12 additional algorithms, also provided by Chenouard et al., was included for comparison. Five different estimators regarding the performance of the algorithms were calculated. The left y-axis refers to  $\alpha$ ,  $\beta$ , JSC and  $JSC_t$ , the right to RMSE. A description for these estimators is given in Section 2.4.4. Evaluation of Tracking Algorithm.

### 3.3.2 Diffusion Analysis of TCR $\beta$ and $\zeta$

(spt)PALM imaging of  $\zeta$ -mEos was performed in murine T cells and extended by simultaneously tracking TCR $\beta$  labelled with scFv-STAR635. Interestingly, I obtained a twofold faster diffusion for  $\zeta$  ( $D \approx 0.114 \pm 0.0035 \mu\text{m}^2/\text{s}$ , Figure 24A) by sptPALM than for TCR $\beta$  by SMT ( $D \approx 0.043 \pm 0.0023 \mu\text{m}^2/\text{s}$ , Figure 24C).

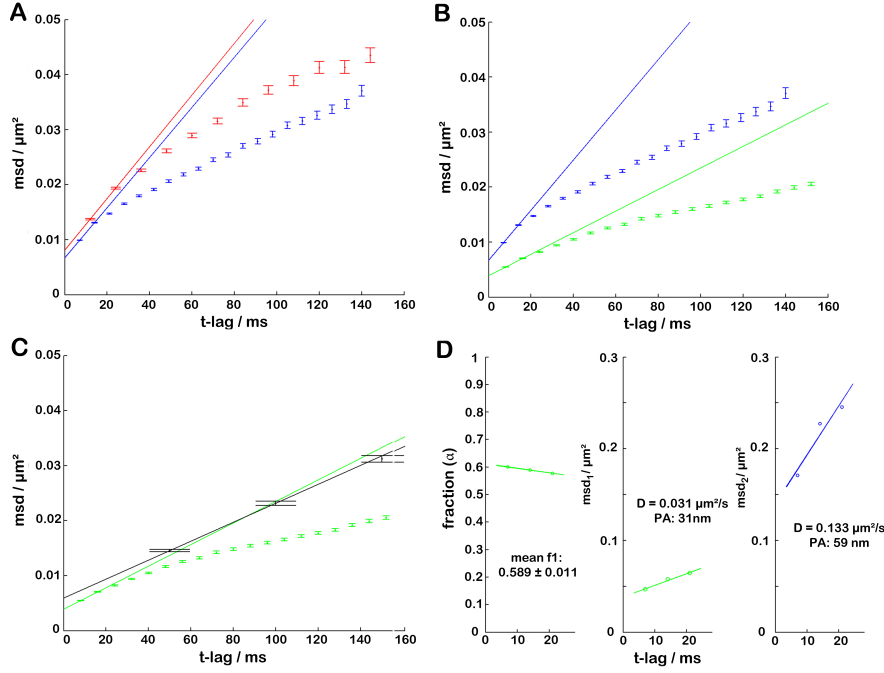


Figure 24: A) Plots of the MSD over time for Jurkat- $\zeta$ -mEos (red) and primary murine T cells infected with  $\zeta$ -mEos (blue) measured by sptPALM. Diffusion coefficients were calculated by using the first two time lags and yielded  $0.118 \pm 0.0044 \mu\text{m}^2/\text{s}$  and  $0.114 \pm 0.0035 \mu\text{m}^2/\text{s}$  respectively. B) Plots of the MSD over time for primary murine T cells labelled with TCR $\beta$ -CAGE635 (green). The diffusion coefficient ( $D \approx 0.049 \pm 0.0026 \mu\text{m}^2/\text{s}$ ) was determined similarly as in A and is lower than for  $\zeta$ -mEos. For comparison, blue symbols show the data depicted in A for primary murine T cells infected with  $\zeta$ -mEos. C) Plots of the MSD over time for primary murine T cells labelled with TCR $\beta$ -STAR635 (black) determined by SMT. The diffusion coefficient ( $D \approx 0.043 \pm 0.0023 \mu\text{m}^2/\text{s}$ ) was similar as determined for sptPALM experiments using TCR $\beta$ -CAGE635. For comparison, green symbols show the data depicted in B primary murine T cells labelled with TCR $\beta$ -CAGE635. D) result of a bi-exponential fitting of the  $\zeta$ -mEos sptPALM tracks yielding a slower fraction of about 60% with a D of  $\approx 0.031 \mu\text{m}^2/\text{s}$ , hence being in the same regime as the D's estimated for TCR $\beta$ , and a faster fraction with a D of  $0.133 \mu\text{m}^2/\text{s}$ .

In order to verify the reliability of sptPALM measurements and analysis, sptPALM measurements were performed for TCR $\beta$  labelled with scFv-CAGE635. A similar diffusion coefficient to the one determined with SMT was measured ( $D \approx 0.049 \pm 0.0026 \mu\text{m}^2/\text{s}$ ).

Cell	Probe	Method	D [ $\mu\text{m}^2/\text{s}$ ]	# of Tracks	# of Cells
Primary Murine T	$\zeta$ -mEos	sptPALM	0.114	19140	48
Primary Murine T	TCR $\beta$ -STAR635	SMT	0.043	1107	9
Jurkat	$\zeta$ -mEos	sptPALM	0.118	6495	9
Primary Murine T	TCR $\beta$ -CAGE635	sptPALM	0.049	4238	18

Table 2: Overview of the different determined diffusion coefficients for  $\zeta$  and TCR $\beta$ , with the respective method and the number of analyzed tracks and the number of analyzed cells.

sptPALM experiments on stably transfected Jurkat- $\zeta$ -mEos cells yielded a diffusion coefficient of  $\zeta$ -mEos ( $D \approx 0.118 \pm 0.0044 \mu\text{m}^2/\text{s}$ ) resembling the one determined on primary murine T cells. A bi-exponential fit (Figure 24D) revealed two fractions of  $\zeta$ -mEos with different properties concerning their mobility. A slower ( $D \approx 0.031 \mu\text{m}^2/\text{s}$ ) yet not fully immobile fraction, for up  $58.9 \pm 1.1\%$  of the  $\zeta$ -mEos molecules, and a faster one ( $D \approx 0.133 \mu\text{m}^2/\text{s}$ ).

### 3.4 Cluster Analysis

After merging the localizations using a dark-time of 0.5 s and  $d_{max}$  of the median PA (25 – 50 nm), Ripley’s K Analysis was performed. This was done in live and fixed cells as well as on activating and non-activating bilayers. An example for the Ripley’s K analysis is depicted in Figure 25. The results for the transduced  $\zeta$ -mEos and the externally labelled TCR $\beta$ -CAGE635 are shown in Figure 26.

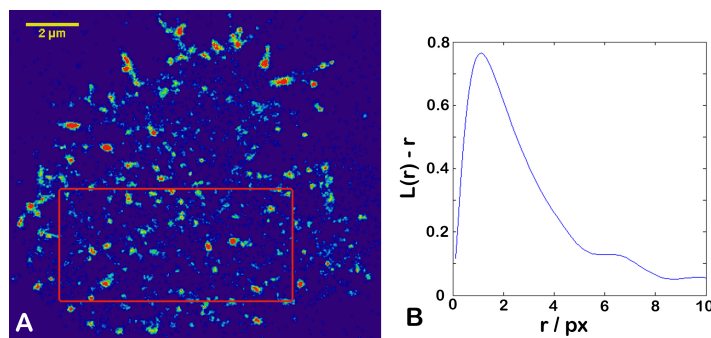


Figure 25: A) PALM image of a fixed murine T cell transfected with  $\zeta$ -mEos and respective ROI selection for Ripley’s K analysis. B) corresponding  $L(r) - r$ , showing significant clustering within a radius of  $\approx 180$  nm and a maximum value of  $\approx 0.75$ .

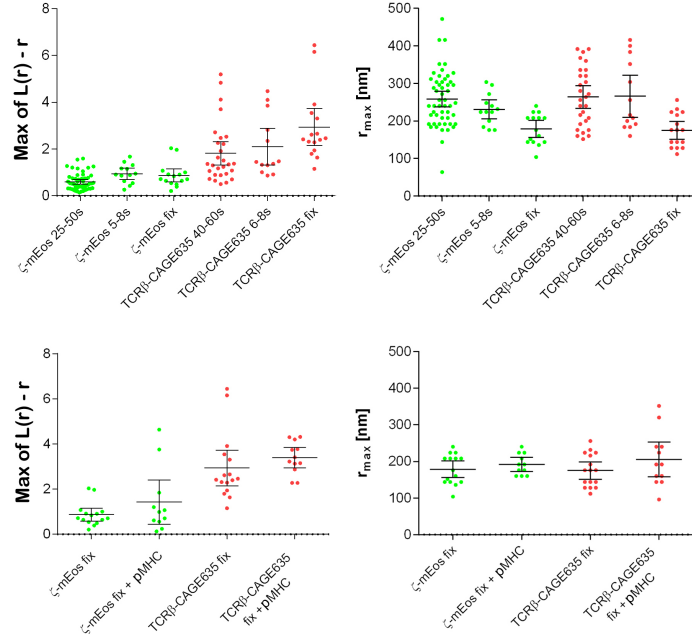


Figure 26: Results of the Ripley's K analysis of live and fixed T cells. Top row: influence of acquisition time in live cell PALM: the maximum values of  $L(r)$ - $r$  increase with shorter acquisition time, or when observing fixed cells. In contrast,  $r_{max}$  decreases. This indicates a reduced extent of smearing of the clusters by the reduction in the protein mobility. Bottom row: results of Ripley's K analysis on fixed T cells on activating and non-activating bilayers. By including pMHC into the bilayers, the maximum value of  $L(r)$ - $r$  as well as  $r_{max}$  increases slightly.

The maximum values of  $L(r)$ - $r$  are significantly higher for  $TCR\beta$ -CAGE635 compared to  $\zeta$ -mEos (2.94 and 0.87, respectively), whereas the distance at which maximum clustering occurs ( $r_{max}$ ) is equal ( $175\pm 44.8$  nm and  $179\pm 40.9$  nm, respectively). For both, the maximum values of  $L(r)$ - $r$  increase with decreasing observation time or when observing fixed cells, whereas  $r_{max}$  decreases.

In experiments using activating bilayers with cell fixation after 20 minutes of incubation, a slight increase in the maximum of  $L(r)$ - $r$  of  $TCR\beta$ -CAGE635 (2.94 to 3.39) as well as of  $\zeta$ -mEos (0.87 to 1.43) was observed. Also the mean value of  $r_{max}$  increased slightly from  $175\pm 44.8$  nm to  $205\pm 74.7$  nm for  $TCR\beta$ -CAGE635 and from  $178\pm 40.9$  nm to  $192\pm 28.6$  nm for  $\zeta$ -mEos.

The localizations were further examined with regard to their temporal occurrence to test the suitability of the chosen parameters for the merging. A color-coded scatter plot of the frame number is shown in Figure 27.

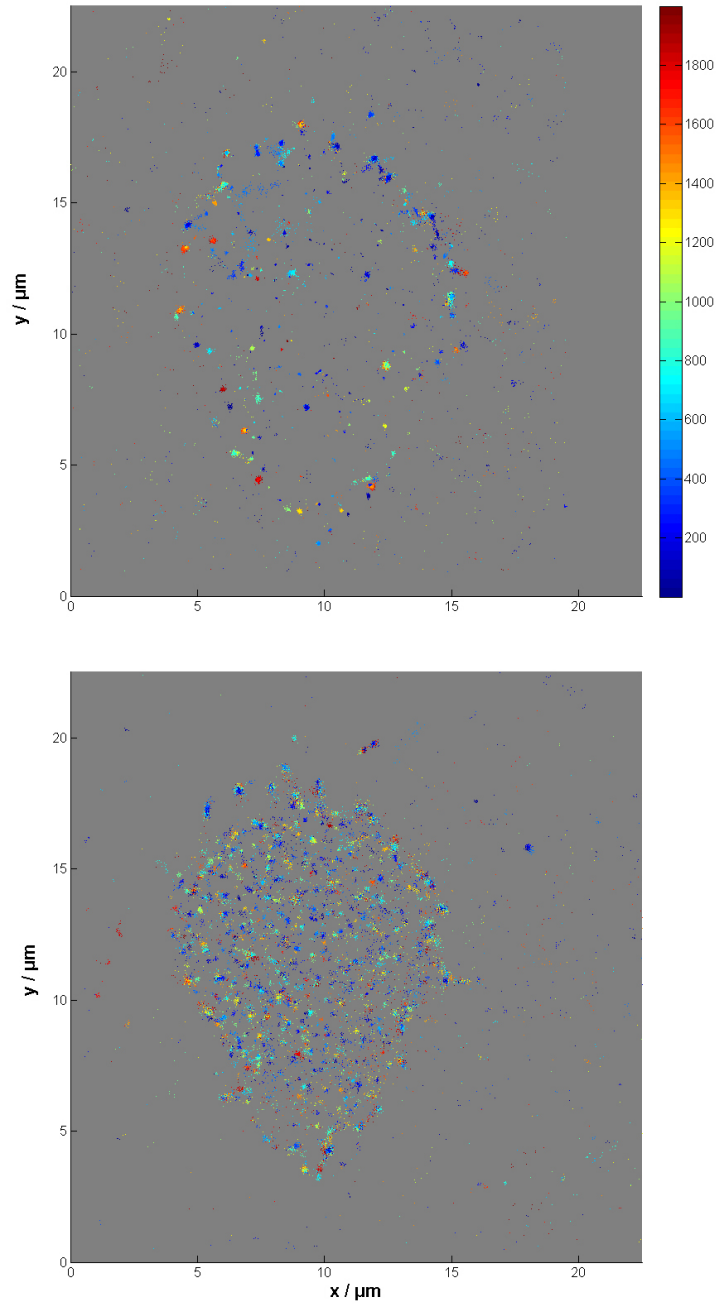


Figure 27: Plot of all localizations of a fixed  $\zeta$ -mEos infected murine T cell, the color-coding of the frame number is indicated by the color-bar. TCR $\beta$ -CAGE635 localizations are shown in the upper image, and  $\zeta$ -mEos is depicted in the image below. The dominance of dark blue points is mainly due to two reasons: i) later localizations are plotted before earlier ones, hence, the earlier ones may cover them, and ii) in the earlier frames, more localizations are recorded, as there are more proteins, which can be activated. Nevertheless, objective evaluation for these images is challenging.

However, the images obtained by this analysis are hard to evaluate by eye. Therefore, the x-coordinates of localizations were depicted over time, as shown in Figure 28. This analysis revealed temporal clustering of the localizations when applying the merging parameters of  $t_{dark} = 0.5$  s and  $d_{max}$  of the median PA (25 - 50 nm).

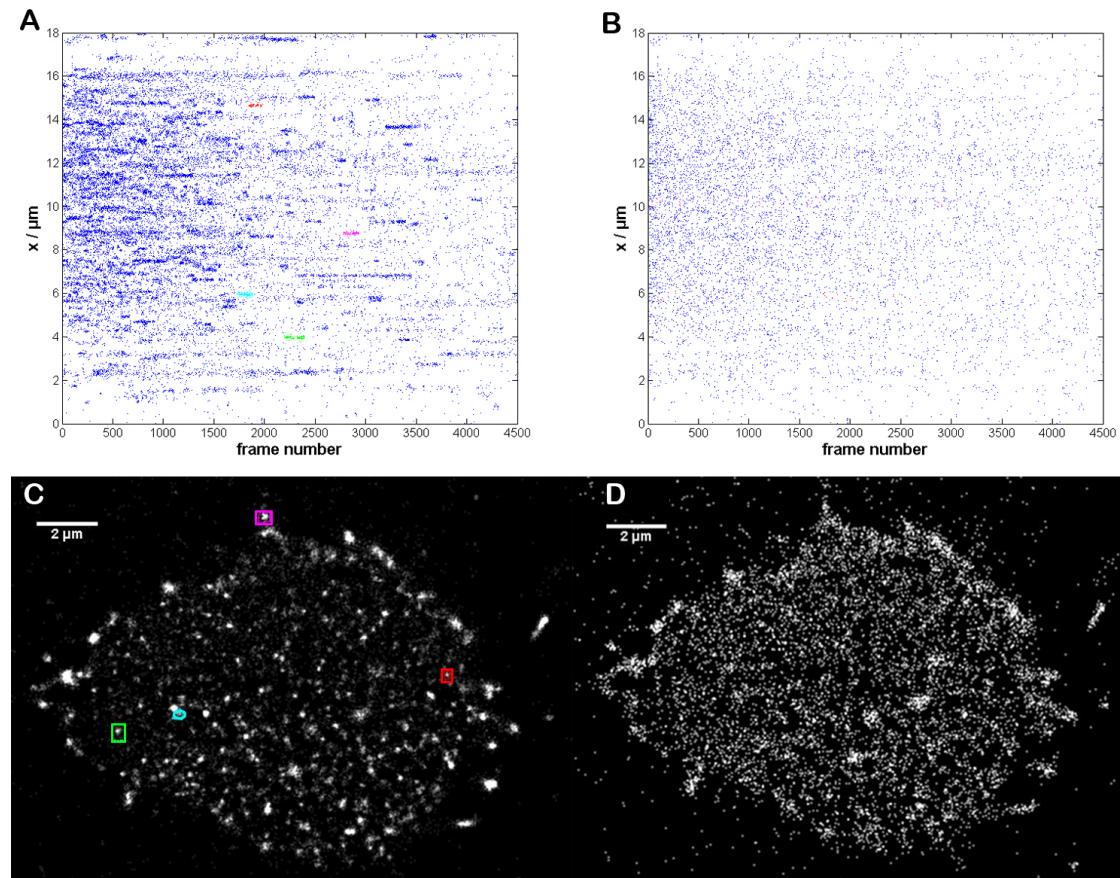


Figure 28: A) kymograph of  $\zeta$ -mEos of the fixed cell shown below (C). The temporal clustering of several selected spatial clusters (green, cyan, magenta and red) in merged images ( $t_{dark} = 0.5$  s,  $d_{max} = 25$ -50 nm) can be seen. B) kymograph after merging with a  $t_{dark} = 2$  s and a  $d_{max} = 100$  nm. The temporal clusters clearly disappear. D) PALM image after merging. The effect is also visible for TCR $\beta$ -CAGE635 and even more pronounced.

The cluster analysis on fixed cells was repeated with increased parameters for the merging algorithm. The results are shown in Figure 29 and compared to the results obtained when using lower temporal and spatial thresholds.

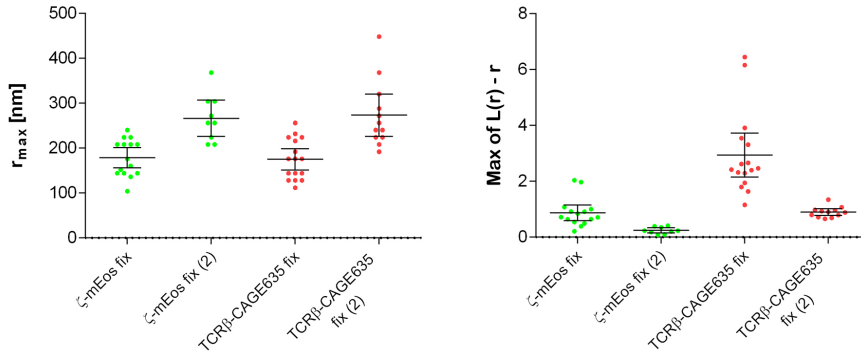


Figure 29: Results of Ripley's K analysis on fixed murine T cells for  $\zeta$ -mEos (green) and TCR $\beta$ -CAGE635 (red). The two sets of utilized merging parameters are compared: (1) represents the values of  $t_{dark} = 0.5$  s and  $d_{max} = 25 - 50$  nm and (2)  $t_{dark} = 2$  s and  $d_{max} = 100$  nm. The increase in the range of maximal clustering for both proteins is shown to the left. The maximum value of  $L(r)-r$  decreased for both proteins, as indicated on the right.

Clustering of TCR $\beta$ -CAGE635 as well as of  $\zeta$ -mEos could still be detected. However, the clustering disappeared in 25% and 40% of the cells, respectively. Furthermore, the maximum values of  $L(r)-r$  were reduced to 28-30% and  $r_{max}$  increased 1.5-1.6 fold.

In order to determine optimal fitting parameters for the merging algorithm, a method proposed by Annibale et al. [115] and adapted by Rossy et al. [55] was used. The resulting plots of the localisations over varying dark times is shown in Figure 30. The fit revealed stronger blinking for mEos with on average 0.99 blinks ( $n_{blink1}$ ) per 25 frames ( $t_{off1}$ ) and 0.31 blinks ( $n_{blink2}$ ) per 0.94 frames ( $t_{off2}$ ), than for CAGE635 with 0.71 blinks ( $n_{blink1}$ ) per 12.5 frames ( $t_{off1}$ ) and 0.18 blinks ( $n_{blink2}$ ) per 0.42 frames ( $t_{off2}$ ). These results suggest the use of  $t_{dark}$  of 30 frames for mEos and 15 frames for CAGE635. For  $d_{max}$ , half the pixel size was used (80 nm). The extracted number of present molecules was 14220 and 7737 for  $\zeta$ -mEos and TCR $\beta$ -CAGE635, respectively.

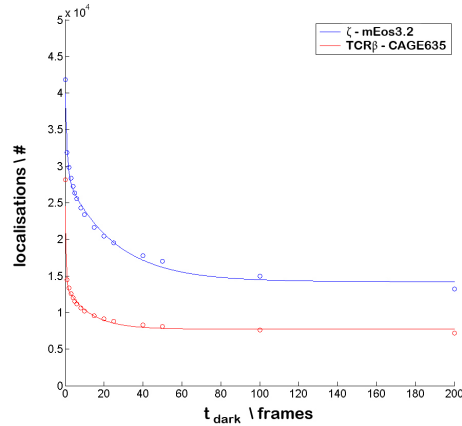


Figure 30: Evaluation of the blinking characteristics from mEos3.2 and CAGE635, using the method described by Annibale et al. In blue the number of localisations are plotted versus dark-times for  $\zeta$ -mEos, whereas red represents TCR $\beta$ -CAGE635. The values are based on 2 independent experiments with a total of 21 - 25 cells. The fit to Equation 11 is represented by the solid lines.

Ripley's K Analysis again revealed clustering, with maximum  $L(r)$ - $r$  and  $r_{max}$  values between the previously determined ones. However, when examining the kymographs of the PALM images, merged with those parameters, obvious temporal clustering was not visible any more (see Figure 31).

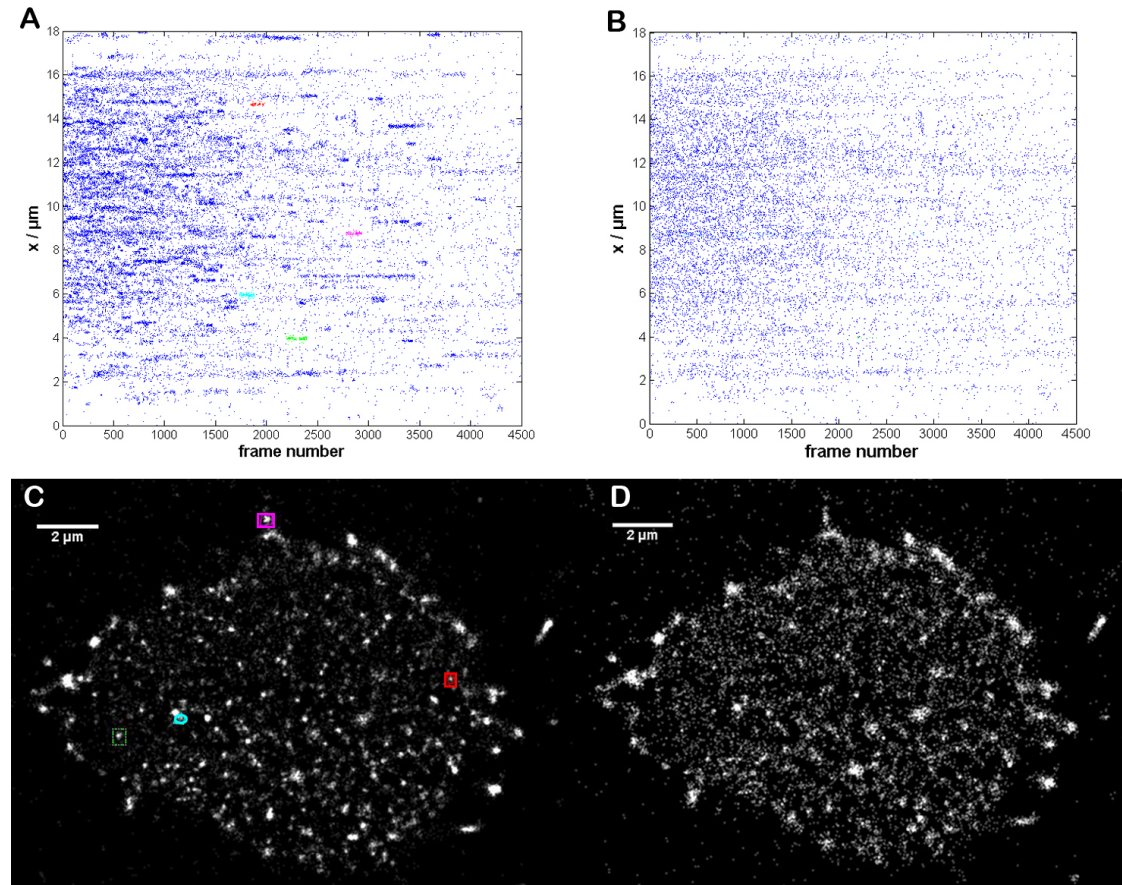


Figure 31: A) kymograph of  $\zeta$ -mEos of the fixed cell shown below (C). The temporal clustering of several selected spatial clusters (green, cyan, magenta and red) in merged images ( $t_{dark} = 0.5$  s,  $d_{max} = 25$ -50 nm) can be seen. B) kymograph after merging with a  $t_{dark} = 0.35$  s and a  $d_{max} = 80$  nm. The temporal clusters again clearly disappear, whereas the spatial clustering in D persists. D) PALM image after merging.

$d_{max}$ [nm]	$t_{dark}$ [s]	mean $r_{max}$ [nm]	mean $\max(L(r)-r)$ [px]	% of cells with clustering	bilayer	probe	fixed/live
25-50	0.5	179 ± 41	0.8738 ± 0.51	100	n.a.	ζ-mEos	fixed
80	0.35	224 ± 39	0.4321 ± 0.20	81	n.a.	ζ-mEos	fixed
100	2	267 ± 52	0.2432 ± 0.12	60	n.a.	ζ-mEos	fixed
25-50	0.5	175 ± 45	2.9407 ± 1.48	100	n.a.	TCR <sub>β</sub> -CAGE635	fixed
80	0.35	224 ± 32	2.7424 ± 1.16	94	n.a.	TCR <sub>β</sub> -CAGE635	fixed
100	2	257 ± 52	0.8782 ± 0.19	69	n.a.	TCR <sub>β</sub> -CAGE635	fixed
25-50	0.5	258 ± 74	0.6022 ± 0.36	-	n.a.	ζ-mEos	live*
25-50	0.5	231 ± 42	0.9426 ± 0.41	-	n.a.	ζ-mEos	live**
25-50	0.5	179 ± 41	0.8738 ± 0.51	100	n.a.	ζ-mEos	fixed
25-50	0.5	264 ± 78	1.8189 ± 1.28	-	n.a.	TCR <sub>β</sub> -CAGE635	live*
25-50	0.5	266 ± 93	2.1039 ± 1.29	-	n.a.	TCR <sub>β</sub> -CAGE635	live**
25-50	0.5	175 ± 45	2.9407 ± 1.48	100	n.a.	TCR <sub>β</sub> -CAGE635	fixed
25-50	0.5	192 ± 29	1.4320 ± 1.46	-	act. <sup>+</sup>	ζ-mEos	fixed
25-50	0.5	179 ± 41	0.8738 ± 0.51	100	n.a.	ζ-mEos	fixed
25-50	0.5	205 ± 75	3.3914 ± 0.71	-	act. <sup>+</sup>	TCR <sub>β</sub> -CAGE635	fixed
25-50	0.5	175 ± 45	2.9407 ± 1.48	100	n.a.	TCR <sub>β</sub> -CAGE635	fixed

Table 3: Summary of the results obtained by Ripley's K analysis for the different merging parameters used for all different experimental settings and probes. \*) the total acquisition time of 25 – 60 s was used for analysis \*\*) only the first 1000 frames (5 – 8 s) were used for analysis +) cells were incubated for 20 minutes on an activating bilayer (including ICAM1, B7-1, pMHC). n.a. = non activating. The first panel highlights the increase in  $r_{max}$  for increasing merging parameters, as well as the decrease in the maximal values of  $L(r)-r$  and the percentage of cells with detectable clustering. The second panel highlights the influence of acquisition time, as the  $r_{max}$  gets smaller with shorter acquisition time and fixation, whereas the maximal  $L(r)-r$  increases. The last panel shows the comparison of values determined for fixed cells on non-activating and activating bilayers, with slight increases in the  $r_{max}$  as well as the maximal values of  $L(r)-r$ . The data is derived from 11 – 52 different cells.

# Chapter 4

## Discussion

### 4.1 $\text{Ca}^{2+}$ Measurements

The T cells were tested on their potency to initiate  $\text{Ca}^{2+}$  flux upon pMHC-binding. Unlabelled pMHC as well as pMHC-A647 and pMHC-A555 were shown to initiate  $\text{Ca}^{2+}$  flux, when included in ICAM1 and B7-1 containing lipid bilayers. The infection of  $\zeta$ -mEos did not affect the pMHC-based initiation of  $\text{Ca}^{2+}$  flux. By addition of Blasticidine after infection, mostly  $\zeta$ -mEos positive cells survived. The acquisition of images of the non-photo-activated  $\zeta$ -mEos, further ensured the analysis of infected T cells only.

The designed software to extract the percentage of cells which undergo  $\text{Ca}^{2+}$  flux as well as their ratio tracks, is able to give a first idea about the characteristics of the surfaces/cells. However, if a more detailed analysis of the particular  $\text{Ca}^{2+}$  ratio tracks is anticipated, certain improvements have to be implemented. Due to the underlying feature-extraction algorithm (circular Hough transform), only circular objects are recognized. The algorithm is hereby very selective, hence, many cells in images recorded with a 100x objective are not identified, yielding gaps within the ratio tracks. For a detailed analysis and classification, these gaps have to be eliminated. This can be accomplished by e.g. applying interpolation steps, or repeating a less sensitive search locally around the cell in consecutive frames.

### 4.2 Evaluation of Localisation and Tracking Algorithm

The evaluation of the used localisation and tracking algorithms enabled the identification of conditions in which it is advisable to employ different algorithms, i.e. in high

density images ( $>3.81 \cdot 10^{-3}$  loc/px<sup>2</sup>) and images with high SNRs ( $>7$ ). However, for the conditions used within this work, the application of the localisation algorithm featured by *thunderSTORM* [110] with consecutive tracking by the algorithm proposed by Gao et al. [101] led to good results. In particular, these conditions are low to mid density (simulation:  $0.4 \cdot 10^{-3}$  -  $1.9 \cdot 10^{-3}$  loc/px<sup>2</sup>, TCR $\beta$ -CAGE635:  $0.4 \cdot 10^{-3}$  loc/px<sup>2</sup> and  $\zeta$ -mEos:  $0.8 \cdot 10^{-3}$  loc/px<sup>2</sup>) in single images and SNRs of 2-4.

The comparison of the two evaluated algorithms to the results presented by Chenouard et al. has to be treated with caution, as most participants spent several months to adapt their algorithms to these randomized test samples. In contrast to that, the settings here were adjusted only roughly to the test samples. The comparison was mainly carried out to identify differences between the localisation of *particle\_tracking\_2D* and *thunderSTORM*. However, *particle\_tracking\_2D* offers up to 7 parameters to be adjusted to the respective dataset for the localization of peaks within an image. The optimization of those parameters to the experimental data has to be ensured. This is challenging for an increasing number of parameters. *thunderSTORM*, on the other hand, keeps the number of user-selected parameters low, hence simplifies the optimization of the localization process for the user, and reduces influences of inappropriate selection of parameters. The differences found between the two tested algorithm combinations could therefore be explained partly by the non-optimal selection of the numerous parameters within the localization algorithm provided by *particle\_tracking\_2D*.

Recently, the results of a challenge held at the International Symposium on Biomedical Imaging in 2013 on the localization of single molecules were published and confirmed the good performance of *thunderSTORM* in images with the above stated properties [119].

### 4.3 Differences in the Diffusion of TCR $\beta$ and $\zeta$

Up to now the mobility of the TCR and/or  $\zeta$  in T cells has been studied very rarely, with differences in the estimates for the diffusional coefficient ranging from  $0.01 \mu\text{m}^2/\text{s}$  detected by FRAP up to  $0.5 \mu\text{m}^2/\text{s}$  estimated by Fluorescence Correlation Spectroscopy (FCS) [51]. Those differences might be introduced by the bias of specific methods towards more mobile or immobile fractions of the proteins. For example, the diffusion coefficient of  $0.5 \mu\text{m}^2/\text{s}$  for  $\zeta$  determined by FCS [51], highlights the bias of this method towards a faster diffusing fraction, whereas slower ones will reach the observation volume less likely. For direct fluorescent video microscopy, like FRAP and PALM, the inverse is true, as faster moving fractions will be identified less likely. This is due to the fact,

that a fast molecule might move significantly during the acquisition time of a single frame, therefore reducing the amount of emitted photons in a single pixel, eventually even below the background level [120].

Already in 1997, Sloan-Lancaster et al. described a low mobility of the intracellular and transmembrane parts of  $\zeta$  fused to the extracellular part of the IL-2 receptor  $\alpha$  chain and GFP by FRAP [121]. However,  $\zeta$ -chimeras were shown to not always represent the biological function of  $\zeta$  [122]. In 2008, Dushek et al. determined the mobility of CD3 $\epsilon$  in varying CD4<sup>+</sup> T cell populations to  $D=0.035\text{-}0.061 \mu\text{m}^2/\text{s}$ , again via FRAP [123]. Those values correspond well with the  $D$  determined for the TCR $\beta$  within this work ( $D \approx 0.041 - 0.052 \mu\text{m}^2/\text{s}$ ). However, I found out that  $\zeta$  has an additional fraction of about 40% that diffuses faster ( $D \approx 0.133 \mu\text{m}^2/\text{s}$ ). Similarly, Sloan-Lancaster et al. observed differences in the diffusion of membrane-associated ZAP-70 and  $\zeta$ -chimeras [121], although those two were believed to interact quite stably, as observed by immunoprecipitation [124]. The data provided within this work hints to more dynamic interactions of TCR/CD3 and  $\zeta$  than previously thought.

The presence of free  $\zeta$  at the plasma membrane is supported by the report of water molecules stabilizing helical transmembrane proteins [125]. Petruk et al. reported the reachability of the negative charges of the  $\zeta$ -dimer by up to six water molecules determined by molecular dynamics simulations [126]. This hydration not only stabilizes the dimer itself, but also enables the interaction with the TCR. Furthermore,  $\zeta$  possesses three positive charges on the intracellular juxtamembrane part, in addition to one negative charge. Electrostatic interactions of those positive charges with the inner leaflet of the membrane, as well as the binding of the ITAMs to the inner leaflet [14], could stabilize free  $\zeta$  within the membrane, and thus support the idea of a TCR/CD3-independent  $\zeta$ .

#### 4.4 Apparent Clustering of TCR $\beta$ and $\zeta$ Determined by PALM

The detection of clustering within SMLM images is a very challenging task. Since for these analyses absolute numbers of molecules are utilized, over- and under-counting represent crucial issues. Photo-activatable and uncageable proteins should theoretically not be able to experience repeated excitation. However, e.g. mEos2 was shown to enter a reversible off-state after being imaged [114]. A potential way to overcome this effect, which was also studied within this work, is to utilize the time dependency in the blinking

of the fluorophores and to merge the detected signals, imaged within a certain spatial and temporal threshold, to a single one. Several methods to extract the optimal parameters have been proposed ([115], [116], [127]).

In this study, different sets of threshold pairs were used, based on the selection previously performed by other groups. The results of Ripley's K analysis were analyzed and the suitability of the thresholds was examined.

In this way, clustering of TCR $\beta$  and  $\zeta$  was detected, and could not be eliminated completely by using more rigorous merging thresholds. Thus, the apparent clustering is not solely based on the multiple localizations of single molecules, however, as the results from Ripley's K analysis show, this issue leads to an over-estimation regarding the pronouncement of clusters and an under-estimation regarding their apparent size.

First, low thresholds were used as stated by Lillemeier et al. and Roh et al. ([51], [58]). With the use of these parameters, clustering of TCR $\beta$ ,  $\zeta$ , Lat and CD4 was identified. Consistent with that, clustering of TCR $\beta$  and  $\zeta$  to approximately the same extent was determined within my work. Nevertheless, after examining the temporal characteristics of these clusters, the clustering could be linked to the continued imaging of single molecules. While this is a requirement for performing sptPALM analysis, it has to be avoided rigorously in quantitative cluster analysis. A  $d_{max}$  of approximately the median PA (25-50 nm) used for merging, seems to be inappropriate and incapable of eliminating multiple detections. In the aforementioned works,  $d_{max}$  was chosen at half the size of a pixel (80 nm), thereby this effect should have been overcome. However, as only localisations in consecutive frames were merged in these works, the blinking of the used fluorophore, i.e. PS-CFP2, could have contributed to over-counting and an over-estimation of clustering.

Independent of the veracity of those clusters and their determined characteristics, I performed Ripley's K analysis on live and fixed cells as well as on activating and non-activating bilayers.

The fact that the range of maximal clustering decreased when performing experiments with shorter observation times or when using fixed cells, highlights the influence of PALM-acquisition in live cells. The reciprocal dependency for the maximal value of  $L(r)$ - $r$  represents the suppression of the broadening of clusters by the proteins movements; hence, fixed cells show a more pronounced clustering. Upon activation with pMHC, the distance of maximal clustering increased slightly for both  $\zeta$  and TCR $\beta$ , as did the maximum values of  $L(r)$ - $r$ . Saito et al. showed micro-cluster formation of  $\zeta$ -EGFP as early as 5 seconds after first cell contact to an activating bilayer, and full cSMAC formation after 5 – 10 minutes [128]. In the PALM images examined in my work no cSMACs were

visible even after 20 minutes. As the potency of the pMHC-bilayer to induce  $\text{Ca}^{2+}$  flux was shown, the activating capability of the bilayer was assumed, however, as these two responses could occur independently, the ability of the T cells to create a cSMAC has to be checked. Assuming this ability, the temperature of incubation after addition of the cells to the bilayer could be responsible for the difference in time-scales between this work and the one by Saito et al. [128]. This is supported by the fact, that Saito et al. stated full cell spreading 60 seconds after first contact, whereas within my work, this was observed to take longer. Due to these considerations, the incubation time of 20 minutes, combined with incubation at room temperature and buffer temperature of  $4^{\circ}\text{C}$  could be too short to perceive any significant differences in clustering of  $\zeta$  and  $\text{TCR}\beta$  between activating and non-activating bilayers.

Second, high merging thresholds were chosen ( $d_{max} = 100$  nm,  $t_{dark} = 2$  s). When examining the kymographs of the images obtained with these thresholds, the temporal clustering completely disappeared. Ripley's K analysis still revealed clustering, however, not in all cells any more, and to a lesser extent, i.e. larger radius of apparent clustering and lower maximal values of  $L(r)-r$ . By this extensive merging, nevertheless, another problem might become apparent: the under-counting of proteins. Several reasons can be responsible for this: antibody-labelling could, due to the size of the antibody and steric hindrance, prevent some proteins from being labelled. This issue, however, is most likely not the case if using scFvs. When employing genetically encoded fluorescence proteins, under-counting might be caused by other factors, e.g. a slow maturation of the used chromophore. Considering an extreme scenario: If the maturation time of the chromophore exceeds the time-span from a membrane proteins translation, the transport to the membrane and to final endocytosis and degradation, no fluorescent signals will be observed within the TIRF illumination field at all. Furthermore, for a complete image of the protein distribution, all proteins have to be imaged exhaustively. This can be examined by plotting the cumulative number of localisations over the frames [129]. However, these localisations might still not resemble the full population of proteins, as some studies determined the number of photo-activated proteins to approximately only 40-60% of total proteins ([130], [131], [132]).

Third, theoretically optimal thresholds for merging were extracted by a method proposed by Annibale et al., as explained in Section 2.4.5. Merging was applied using dark-times of 0.35 s and 0.15 s for mEos and CAGE635, respectively, and a  $d_{max}$  of half the pixel size (80 nm). This method was also used by Rossy et al. to show spatial nano-clustering of Lck [55]. When performing Ripley's K analysis on these images, clustering to an extent between the thresholds examined before was identified. The kymographs also revealed

obvious elimination of temporal clustering of the localisations, thereby highlighting the power of the above mentioned method to extract a fluorophore’s blinking characteristics, and its successful application to eliminating clustering artefacts introduced by multiple detection of single molecules.

Within this work the cluster analysis using increased merging parameters still revealed clustering. The difference in maximal values of  $L(r)$ - $r$  between  $\zeta$  and TCR $\beta$  fits into the idea of additional TCR/CD3-independent  $\zeta$  within the membrane. This free  $\zeta$  may be responsible for the lower values of  $L(r)$ - $r$  as it reduces the cluster-like appearance in PALM images.

Taken together, a well-grounded selection of the merging parameters was shown to be crucial for a reliable quantitative analysis of SMLM images. Those parameters depend heavily on the used fluorophore and the utilized acquisition protocol. Therefore, the Ripley’s K results as well as many published data have to be seen cautiously ([51], [55], [58], [133]). In addition to that, several studies have been published before many of the difficulties of data analysis have been worked out in detail, so the results on apparent clustering derived by SMLM methods should be treated very tentatively.

## 4.5 Further Aspects and Outlook

### Effects of the Transduction of $\zeta$ -mEos

The findings within this work indicate TCR/CD3-unbound  $\zeta$  within the membrane of primary murine T cells. However, it still has to be ensured, that the differences found in the proteins mobility, are not due to the introduction of exogenous  $\zeta$ . This issue can be tackled by tracking the  $\zeta$  on wild-type T cells. However, due to a lack of supply of antibodies against the short, extracellular part of  $\zeta$ , this was so far not achievable. The introduction of  $\zeta$ -mEos into  $\zeta$ -deficient MA5.8 T-cells facilitates the circumvention of a potential experimental bias caused by endogenous  $\zeta$ . Nevertheless, possible over-expression of the exogenous  $\zeta$ -mEos can still not be excluded. A very recently proposed method to overcome the issues of over-expression and possible bias by endogenous, unlabelled proteins is based on genetic knock in modification using the CRISPR/Cas9 genome editing system [134]. Ratz et al. demonstrated this method on three different gene loci encoding for proteins localizing to different compartments (nucleus, cytoskeleton, plasma membrane) in live human cells and accomplished consecutive super-resolution imaging by using RESOLFT [135]. Still, the application of the CRISPR/Cas9 genome editing

system takes considerably time, exceeding the life span of primary murine T cell blasts, used in this work, hence this method is restricted to cell lines, e.g. the Jurkat cell line.

### **Experiments on the Interaction Kinetics of TCR/CD3 and $\zeta$**

The interaction kinetics between  $\zeta$  and the TCR/CD3 complex can be examined by a recently developed method, using micro-patterning of antibodies printed on epoxy-slides. Hereby, the interactions between a fixed *prey* protein (e.g. anti-CD3 $\epsilon$ ) and a free membrane protein (*bait*, e.g.  $\zeta$ ) can be studied. Associations can be examined by analyzing co-localization of the bait protein and the prey. Additionally, FRAP experiments on patterned surfaces can further provide information on the interaction dynamics of both proteins ([136], [137]).

### **Alternative Cluster Analysis**

A further possibility to analyze the images in regard to clustering, and to additionally take the over-counting directly into account within the analysis, can be provided by the application of the pair-wise correlation function as described, e.g. in [138] and [139]. The PCF analysis yields values for clustering at specific distances, whereas Ripley's K analysis returns integral values for clustering of up to certain distances, thus introducing a bias towards larger cluster sizes. With PCF, however, an excellent sample fixation has to be ensured, as short-distance movements would be mistaken as clustering, instead of getting rid of the erroneous over-counting.

### **Other Influences on the Mobility of TCR, CD3 and $\zeta$**

The dependency of the mobility of TCR, CD3 and  $\zeta$  on intracellular  $\text{Ca}^{2+}$  concentration, as well as on the possible association of either of the parts to the Actin cytoskeleton, as shown by Dushek et al. [123], is a further aspect of great interest. A decrease in the TCR/CD3 mobility on  $\text{Ca}^{2+}$  increase was shown and could be linked to the complex becoming associated to Actin.

# Abbreviations

AIDS	Acquired Immune Deficiency Syndrome
AOM	Accusto-optical Modulator
APC	Antigen Presenting Cell
BCR	B Cell Receptor
CD	Cluster of Differentiation
CDF	Cumulative Density Function
CRAC	Calcium Release-Activated Calcium Channels
cSMAC	central Supramolecular Activation Cluster
DAG	diacylglycerol
DMEM	Dulbecco's Modified Eagle Medium
dSTORM	direct Stochastic Optical Reconstruction Microscopy
EGFP	Enhanced Green Fluorescent Protein
EMCCD	Electron Multiplying Charge-Coupled Devices
ER	Endoplasmic Reticulum
FBS	Fetal Bovine Serum
FCS	Fetal Calf Serum
FCS	Fluorescence Correlation Spectroscopy
FN	Fibronectin

FRAP	Fluorescent Recovery After Photobleaching
FRET	Förster Resonance Energy Transfer
GFP	Green Fluorescent Protein
HBSS	Hank's Balanced Salt Solution
HIV	Human Immunodeficiency Virus
ICAM	intercellular adhesion molecules
Ig	Immunoglobulin
IgG	Immunoglobulin G
IL-2	Interleukin-2
IP <sub>3</sub>	inositol 1, 4, 5-triphosphate
ITAM	Immunoreceptor Tyrosine-based Activation Motif
LAT	Linker of activated T cells
LB	Lysogeny Broth
Lck	lymphocyte-specific protein tyrosine kinase
LFA-1	leukocyte functional antigen-1
LS	Least-Squares
mEos	monomeric Eos
MHC	Major Histocompatibility Complex
MLE	maximum likelihood estimation
MUW	Medical University of Vienna
NA	Numerical Aperture
NFAT	Nuclear Factor of Activated T-cells
Ni-DOGS	Nickel chelated 1,2-dioleoyl-sn-glycero-3-[(N-(5-amino-1-carboxypentyl)iminodiacetic acid)succinyl]

PA	Positional Accuracy
PAMP	Pathogen-Associated Molecular Patterns
PBS	Phosphate Buffered Saline
PFA	Paraformaldehyde
PICS	Particle Image Correlation Spectroscopy
PIP <sub>2</sub>	phosphatidylinositol 4, 5-bisphosphate
PLC- $\gamma$	phospholipase C- $\gamma$
pMHC	peptide-Major Histocompatibility Complex
POPC	1-Palmitoyl-2-oleoylphosphatidylcholine
PS-CFP2	Photo-Switchable Cyan Fluorescent Protein
PSF	Point Spread Function
pSMAC	peripheral Supramolecular Activation Cluster
ROI	Region of Interest
scFv	single-chain variable fragment
SIM	Structural Illumination Microscopy
SLP-76	SH2 domain-containing leukocyte protein of 76kDa
SMLM	Single-Molecule Localization Microscopy
SMT	Single Molecule Tracking
SNR	Signal-to-Noise Ratio
sptPALM	single particle tracking Photoactivatable Localization Microscopy
STED	Stimulated-Emission-Depletion Fluorescence Microscopy
STORM	Stochastic Optical Reconstruction Microscopy
TCM	T Cell Medium
TCR	T Cell Receptor

TIRF	Total Internal Reflection Fluorescence
UV	Ultraviolet
YFP	Yellow Fluorescent Protein
ZAP-70	$\zeta$ -chain-associated protein kinase 70

# List of Figures

1	Reported Diphtheria cases since 1900. . . . .	7
2	Cytotoxic T cell interacting with a target cell. . . . .	9
3	IgG Structure. . . . .	10
4	Comparison of IgG and TCR structure. . . . .	11
5	Comparison of CD4/MHC-I and CD8/MHC-II . . . . .	12
6	Clonal Selection Theory. . . . .	13
7	Structure and interactions of the TCR/CD3/ $\zeta$ complex. . . . .	15
8	Structure of the $\zeta$ homodimer. . . . .	16
9	T cell activation pathway. . . . .	18
10	Structure and genetic map of a retro virus. . . . .	21
11	Influence of immersion medium and the imaging path of a microscope. . . . .	23
12	Jablonski diagram for fluorescence, red shift in excitation spectrum and the TIRF illumination. . . . .	25
13	Huygens principle for plane waves and on a single slit. . . . .	26
14	Rayleigh criterion for resolution and non-resolvable dots. . . . .	28
15	Principle and example of PALM/STORM. . . . .	29
16	Description of a MSD-t-plot and its different shapes. . . . .	34
17	Raw data of two-color PALM image. . . . .	40
18	Imaging sequence for PALM and simultaneous SMT. . . . .	41
19	Circular Hough Transform. . . . .	42
20	Ripley's K Analysis Schematic. . . . .	47
21	Calcium Analysis Software. . . . .	50
22	Calcium Flux Results. . . . .	51
23	Results of Tracking Algorithm Evaluation. . . . .	52
24	MSD-t-plots for $\zeta$ and TCR $\beta$ recorded by sptPALM and SMT, and an additional explot for showing two fractions of $\zeta$ . . . . .	53

25	PALM image with its respective Ripley's K analysis. . . . .	54
26	Ripley's K analysis for $\zeta$ and TCR $\beta$ . . . . .	55
27	Color Coded Visualization of TCR $\beta$ -CAGE635 and $\zeta$ -mEos Localisations. . . . .	56
28	Kymographs of different sets of merging parameters for $\zeta$ and TCR $\beta$ and the corresponding PALM images. . . . .	57
29	Comparison of Ripley's K results for different sets of merging parameters . . . . .	58
30	Fit for the dependence of the number of localisations on the merging dark-time. . . . .	58
31	Kymographs of different sets of merging parameters for $\zeta$ and TCR $\beta$ and the corresponding PALM images II. . . . .	59

# List of Tables

1	Tracking Algorithm Parameters. . . . .	43
2	Estimated Diffusion Coefficients. . . . .	54
3	Summary of Ripley's K results. . . . .	60

# Bibliography

- [1] K. Murphy. *Janeway's Immunobiology*. Garland Science, 8th edition, 2012.
- [2] S. J. Walsh and L. M. Rau. Autoimmune diseases: A leading cause of death among young and middle-aged women in the united states. *Am J Pub Health*, 90:1463–66, 2000.
- [3] B. C. Chen et al. Lattice light-sheet microscopy: imaging molecules to embryos at high spatiotemporal resolution. *Science*, 346:1257998, 2014.
- [4] S. S. Pang et al. The structural basis for autonomous dimerization of the pre-t-cell antigen receptor. *Nature*, 467:844–8, 2010.
- [5] R. Blumberg et al. Structure of the t-cell antigen receptor: Evidence for two cd3 $\epsilon$  subunits in the t-cell receptor-cd3 complex. *Proc Natl Acad Sci U S A*, 87:7220–24, 1990.
- [6] A. de la Hera et al. Structure of the t cell antigen receptor (tcr): Two cd3 $\epsilon$  subunits in a functional tcr/cd3 complex. *J Exp Med*, 173:7–17, 1991.
- [7] M. E. Call et al. The organizing principle in the formation of the t cell receptor-cd3 complex. *Cell*, 111:967–79, 2002.
- [8] G. Fernandez-Miguel et al. Multivalent structure of an  $\alpha\beta$ t cell receptor. *Proc Natl Acad Sci U S A*, 96:1547–52, 1999.
- [9] W. W. Schamel and B. Alarcon. Organization of the resting tcr in nanoscale oligomers. *Immunol Rev*, 251:13–20, 2013.
- [10] M. E. Call and K. W. Wucherpfennig. Molecular mechanisms for the assembly of the t cell receptor-cd3 complex. *Mol Immunol*, 40:1295–305, 2004.

- [11] M. S. Kuhns et al. Evidence for a functional sidedness to the  $\alpha\beta$ tcr. *Proc Natl Acad Sci U S A*, 107:5094–9, 2010.
- [12] W. W. Schamel et al. Coexistence of multivalent and monovalent tcers explains high sensitivity and wide range of response. *J Exp Med*, 202:493–503, 2005.
- [13] M. E. Call et al. Stoichiometry of the t-cell receptor-cd3 complex and key intermediates assembled in the endoplasmatic reticulum. *The EMBO J*, 23, 2004.
- [14] K. W. Wucherpfennig et al. Structural biology of the t-cell receptor: insights into receptor assembly, ligand recognition, and initiation of signaling. *Cold Spring Harb Perspect Biol*, 2, 2010.
- [15] E. Teixeira et al. T cell division and death are segregated by mutation of tcr $\beta$  chain constant domains. *Immunity*, 21:515–26, 2004.
- [16] B. T. Bäckström et al. A motif within the t cell receptor  $\alpha$  chain constant region connecting peptide domain controls antigen responsiveness. *Immunity*, 5:437–47, 1996.
- [17] M. S. Kuhns et al. Deconstructing the form and function of the tcr/cd3 complex. *Immunity*, 24:133–9, 2006.
- [18] M. S. Kuhns and M. M. Davis. Disruption of extracellular interactions impairs t cell receptor-cd3 complex stability and signaling. *Immunity*, 26:357–69, 2007.
- [19] Z. Y. Sun et al. Mechanisms contributing to t cell receptor signaling and assembly revealed by the solution structure of an ectodomain fragment of the cd3 $\epsilon\gamma$  heterodimer. *Cell*, 105:913–23, 2001.
- [20] Z. Y. Sun et al. Solution structure of the cd3 $\epsilon\delta$  ectodomain and comparison with cd3 $\epsilon\gamma$  as a basis for modeling t cell receptor topology and signaling. *Proc Natl Acad Sci U S A*, 101:16867–72, 2004.
- [21] M. E. Call et al. The structure of the  $\zeta\zeta$  transmembrane dimer reveals features essential for its assembly with the t cell receptor. *Cell*, 127:355–68, 2006.
- [22] T. Rutledge et al. Transmembrane helical interactions:  $\zeta$  chain dimerization and functional association with the t cell antigen receptor. *EMBO J*, 11:3245–54, 1992.

- [23] J. S. Bonifacino et al. Colocalized transmembrane determinants for er degradation and subunit assembly explain the intracellular fate of tcr chains. *Cell*, 63:503–13, 1990.
- [24] C. Geisler et al. Assembly, intracellular processing, and expression at the cell surface of the human  $\alpha$ - $\beta$  t cell receptor/cd3 complex - function of the cd3 $\zeta$  chain. *J Immunol*, 143:4069–77, 1989.
- [25] Y. Minami et al. Building a multichain receptor: Synthesis, degradation, and assembly of the t-cell antigen receptor. *Proc Natl Acad Sci USA*, 84:2688–92, 1987.
- [26] A. M. Weissman et al. Role of the  $\zeta$  chain in the expression of the t cell antigen receptor: genetic reconstitution studies. *The EMBO J*, 8:3651–56, 1989.
- [27] J. D. Ashwell and R. D. Klausner. Genetic and mutational analysis of the t-cell antigen receptor. *Annu Rev Immunol*, 8:139–67, 1990.
- [28] J. J. Sussman et al. Failure to synthesize the t cell cd3 $\zeta$  chain: Structure and function of a partial t cell receptor complex. *Cell*, 52:85–95, 1988.
- [29] U. D’Oro et al. Regulation of constitutive tcr internalization by the  $\zeta$ -chain. *The Journal of Immunology*, 169:6269–78, 2002.
- [30] S. Ono et al. Rapid turnover of the cd3 $\zeta$  chain independent of the tcr-cd3 complex in normal t cells. *Immunity*, 2:639–44, 1995.
- [31] T. W. F. Göbe and L. Bolliger. Cutting edge: The chicken tcr  $\zeta$ -chain restores the function of a mouse t cell hybridoma. *J Immunol*, 160:1552–54, 1998.
- [32] G. M. Deng et al. T cell cd3 $\zeta$  deficiency enables multiorgan tissue inflammation. *J Immunol*, 191:3563–7, 2013.
- [33] S.-N. C. Liossis et al. Altered pattern of tcr/cd3-mediated protein-tyrosyl phosphorylation in t cells from patients with systemic lupus erythematosus. *J Clin Inv*, 101:1448–57, 1998.
- [34] D. D. Taylor et al. Modulation of tcr/cd3 $\zeta$  chain expression by a circulating factor derived from ovarian cancer patients. *Brit J Canc*, 84:1624–29, 2001.

- [35] X. Chen et al. Impaired expression of the cd3 $\zeta$  chain in peripheral blood t cells of patients with chronic myeloid leukaemia results in an increased susceptibility to apoptosis. *Brit J Haem*, 111:817–25, 2000.
- [36] A. M. Weissman et al. Molecular cloning and chromosomal localization of the human t-cell receptor  $\zeta$  chain: Distinction from the molecular cd3 complex. *Proc Natl Acad Sci U S A*, 85:9709–13, 1988.
- [37] S. Minguet et al. The short length of the extracellular domain of  $\zeta$  is crucial for t cell antigen receptor function. *Immunol Lett*, 116:195–202, 2008.
- [38] L. Bolliger et al. The short extracellular domain of the t cell receptor  $\zeta$  chain is involved in assembly and signal transduction. *Mol Immunol*, 34:819–27, 1997.
- [39] L. Bolliger and B. Johansson. Identification and functional characterization of the  $\zeta$ -chain dimerization motif for tcr surface expression. *J Immunol*, 163:3867–76, 1999.
- [40] S. Caplan et al. Cell-surface-expressed t-cell antigen-receptor  $\zeta$  chain is associated with the cytoskeleton. *Proc Natl Acad Sci U S A*, 92:4768–72, 1995.
- [41] M. Castro et al. Receptor pre-clustering and t cell responses: Insights into molecular mechanisms. *Front Immunol*, 5:132, 2014.
- [42] R. Blanco and B. Alarcon. Tcr nanoclusters as the framework for transmission of conformational changes and cooperativity. *Front Immunol*, 3:115, 2012.
- [43] O. Dushek et al. A role for rebinding in rapid and reliable t cell responses to antigen. *PLoS Comput Biol*, 5, 2009.
- [44] E. Klotzsch et al. Do mechanical forces contribute to nanoscale membrane organisation in t cells? *Biochim Biophys Acta*, 2014.
- [45] J. H. Wang and E. L. Reinherz. The structural basis of alphabeta t-lineage immune recognition: Tcr docking topologies, mechanotransduction, and co-receptor function. *Immunol Rev*, 250:102–19, 2012.
- [46] S. T. Kim et al. Tcr mechanobiology: Torques and tunable structures linked to early t cell signaling. *Front Immunol*, 3:76, 2012.
- [47] D. Aivazian and L. J. Stern. Phosphorylation of t cell receptor  $\zeta$  is regulated by a lipid dependent folding transition. *Nat Struct Bio*, 7:1023–26, 2000.

- [48] G. P. Morris and P. M. Allen. How the tcr balances sensitivity and specificity for the recognition of self and pathogens. *Nat Immunol*, 13:121–8, 2012.
- [49] K.-H. Lee et al. T cell receptor signaling precedes immunological synapse formation. *Science*, 295:1539–42, 2002.
- [50] C. R. F. Monks et al. Selective modulation of protein kinase  $c\text{-}\theta$  during t-cell activation. *Nature*, 385:83–86, 1997.
- [51] B. F. Lillemeier et al. Tcr and lat are expressed on separate protein islands on t cell membranes and concatenate during activation. *Nat Immunol*, 11:90–6, 2010.
- [52] F. Baumgart and G. J. Schutz. Detecting protein association at the t cell plasma membrane. *Biochim Biophys Acta*, 2014.
- [53] B. F. Lillemeier et al. Plasma membrane-associated proteins are clustered into islands attached to the cytoskeleton. *Proc Natl Acad Sci U S A*, 103:18992–7, 2006.
- [54] E. Sherman et al. Functional nanoscale organization of signaling molecules downstream of the t cell antigen receptor. *Immunity*, 35:705–20, 2011.
- [55] J. Rossy et al. Conformational states of the kinase lck regulate clustering in early t cell signaling. *Nat Immunol*, 14:82–89, 2012.
- [56] D. M. Owen et al. Sub-resolution lipid domains exist in the plasma membrane and regulate protein diffusion and distribution. *Nat Commun*, 3:1256, 2012.
- [57] E. Molnar et al. Cholesterol and sphingomyelin drive ligand-independent t-cell antigen receptor nanoclustering. *J Biol Chem*, 287:42664–74, 2012.
- [58] K.-H. Roh et al. The coreceptor cd4 is expressed in distinct nanoclusters and does not colocalize with t-cell receptor and active protein tyrosine kinase p56lck. *Proc Natl Acad Sci U S A*, 2015.
- [59] E. Sherman et al. Super-resolution characterization of tcr-dependent signaling clusters. *Immunol Rev*, 251:21–35, 2013.
- [60] J. Minowada et al. *Characteristics of 27 Human T-Cell Leukemia Cell Lines Without T-Cell Receptors of T3-Ti  $\alpha\beta$  or T3-Ti  $\gamma\delta$  Complex*, volume 32. Springer Berlin Heidelberg, Heidelberg, 1989.

- [61] R. R. Bartelt et al. Comparison of t cell receptor-induced proximal signaling and downstream functions in immortalized and primary t cells. *PLoS One*, 4, 2009.
- [62] D. F. Tough and J. Sprent. Life span of naive and memory t cells. *Stem Cells*, 13:242–49, 1996.
- [63] Wikimedia Commons. Hiv, [http://commons.wikimedia.org/wiki/file:hiv\\_gross.png](http://commons.wikimedia.org/wiki/file:hiv_gross.png), visited on 22.05.2015.
- [64] Wikipedia. Retroviruses - genomic map, <http://de.wikipedia.org/wiki/retroviren>, visited on 22.05.2015.
- [65] J. Holst et al. Generation of t-cell receptor retrogenic mice. *Nat Protoc*, 1:406–17, 2006.
- [66] R. A. Morgan et al. Cancer regression in patients after transfer of genetically engineered lymphocytes. *Science*, 314:126–29, 2006.
- [67] L. J. Berg et al. Antigen/mhc-specific t cells are preferentially exported from the thymus in the presence of their mhc ligand. *Cell*, 58:1035–46, 1989.
- [68] W. S. Pear et al. Production of high-titer helper-free retroviruses by transient tranfection. *Proc Natl Acad Sci U S A*, 90:8392–96, 1993.
- [69] S. Swift et al. Rapid production of retroviruses for efficient gene delivery to mammalian cells using 293t cell-based systems. *Curr Prot Immunol*, 1999.
- [70] S. Bliven. Airy disk spacing near rayleigh criterion, [http://en.wikipedia.org/wiki/angular\\_resolution](http://en.wikipedia.org/wiki/angular_resolution), visited on 22.05.2015.
- [71] U. Kubitscheck. *Fluorescence Microscopy - From Principles to Biological Applications*. Wiley-Blackwell, Weinheim, Germany, 2013.
- [72] Zeiss-Campus. Jablonski diagram, <http://zeiss-campus.magnet.fsu.edu/articles/basics/fluorescence.html>, visited on 22.05.2015.
- [73] abberior. Abberior star635 spectrum, <http://www.abberior.com/products/productlist/cat/confocal-epi-sim/prod/abberior-star-635/>, visited on 22.05.2015.
- [74] Nikon MicroscopyU. High na objective tirfm, <https://www.microscopyu.com/articles/fluorescence/tirf/tirfintro.html>, visited on 22.05.2015.

- [75] E. A. Robinson and D. Clark. Basic seismology 13 - Huygens principle. *The Leading Edge*, 25:1252–55, 2006.
- [76] A. Nordmann. Refraction on an aperture, [http://de.wikipedia.org/wiki/Huygenssches\\_Prinzip](http://de.wikipedia.org/wiki/Huygenssches_Prinzip), visited on 23.05.2015.
- [77] Zeiss-Campus. The Rayleigh criterion, <http://zeiss-campus.magnet.fsu.edu/articles/basics/resolution.html>, visited on 22.05.2015.
- [78] B. Huang et al. Super-resolution fluorescence microscopy. *Annu Rev Biochem*, 78:993–1016, 2009.
- [79] M. G. L. Gustafsson. Surpassing the lateral resolution limit by a factor of two using structured illumination microscopy. *Journal of Microscopy*, 198:82–87, 2000.
- [80] S. W. Hell and J. Wichmann. Breaking the diffraction resolution limit by stimulated emission: stimulated-emission-depletion fluorescence microscopy. *Opt Lett*, 19:780–82, 1994.
- [81] T. A. Klar et al. Breaking Abbe’s diffraction resolution limit in fluorescence microscopy with stimulated emission depletion beams of various shapes. *Physical Review E*, 64, 2001.
- [82] Nikon MicroscopyU. Basic principle of STORM superresolution imaging, <https://www.microscopyu.com/articles/superresolution/stormintro.html>, visited on 22.05.2015.
- [83] Imaging and Microscopy. Live cell super-resolution microscopy with plastic bottom slides, <http://www.imaging-git.com/products/light-microscopy/live-cell-super-resolution-microscopy-plastic-bottom-slides>, visited on 22.05.2015.
- [84] E. Betzig et al. Imaging intracellular fluorescent proteins at nanometer resolution. *Science*, 313:1642–45, 2006.
- [85] M. J. Rust et al. Sub-diffraction-limit imaging by stochastic optical reconstruction microscopy (STORM). *Nat Methods*, 3:793–96, 2006.
- [86] M. Heilemann et al. Subdiffraction-resolution fluorescence imaging with conventional fluorescent probes. *Angew Chem Int Ed Engl*, 47:6172–6, 2008.
- [87] M. Heilemann et al. Carbocyanine dyes as efficient reversible single-molecule optical switch. *J Am Chem Soc*, 127:3801–6, 2005.

- [88] M. Fernandez-Suarez and A. Y. Ting. Fluorescent probes for super-resolution imaging in living cells. *Nat Rev Mol Cell Biol*, 9:929–43, 2008.
- [89] S. A. McKinney et al. A bright and photostable photoconvertible fluorescent protein for fusion tags. *Nat Methods*, 6:131–33, 2009.
- [90] M. Zhang et al. Rational design of true monomeric and bright photoactivatable fluorescent proteins. *Nat Methods*, 9:727–9, 2012.
- [91] C. A. Wurm et al. Novel red fluorophores with superior performance in sted microscopy. *Opt Nano*, 1, 2012.
- [92] V. N. Belov et al. Masked rhodamine dyes of five principal colors revealed by photolysis of a 2-diazo-1-indanone caging group: synthesis, photophysics, and light microscopy applications. *Chemistry*, 20:13162–73, 2014.
- [93] L. D. Hughes et al. Choose your label wisely: water-soluble fluorophores often interact with lipid bilayers. *PLoS One*, 9, 2014.
- [94] A. Small and S. Stahlheber. Fluorophore localization algorithms for super-resolution microscopy. *Nat Methods*, 11:267–79, 2014.
- [95] R. E. Thompson et al. Precise nanometer localization analysis for individual fluorescent probes. *Biophys J*, 82:2775–83, 2002.
- [96] K. I. Mortensen et al. Optimized localization analysis for single-molecule tracking and super-resolution microscopy. *Nat Methods*, 7:377–81, 2010.
- [97] M. Weiss et al. Anomalous subdiffusion is a measure for cytoplasmic crowding in living cells. *Biophys J*, 87:3518–24, 2004.
- [98] G. J. Schütz et al. Single-molecule microscopy on model membranes reveals anomalous diffusion. *Biophys J*, 73:1073–80, 1997.
- [99] S. Manley et al. High-density mapping of single-molecule trajectories with photoactivated localization microscopy. *Nat Methods*, 5:155–7, 2008.
- [100] N. Chenouard et al. Objective comparison of particle tracking methods. *Nat Methods*, 11:281–9, 2014.
- [101] Y. Gao and M. L. Kilfoil. Accurate detection and complete tracking of large populations of features in three dimensions. *Opt Express*, 17:4685–704, 2009.

- [102] S. Semrau and T. Schmidt. Particle image correlation spectroscopy (pics): retrieving nanometer-scale correlations from high-density single-molecule position data. *Biophys J*, 92:613–21, 2007.
- [103] S. Wieser and G. J. Schutz. Tracking single molecules in the live cell plasma membrane-do’s and don’t’s. *Methods*, 46:131–40, 2008.
- [104] A. Radenovic. Brownian motion and single particle tracking.
- [105] S. Wieser et al. (un)confined diffusion of cd59 in the plasma membrane determined by high-resolution single molecule microscopy. *Biophys J*, 92:3719–28, 2007.
- [106] S. Zhong et al. Retroviral transduction of t-cell receptors in mouse t-cells. *J Vis Exp*, 44, 2010.
- [107] D. R. Whelan and T. D. Bell. Image artifacts in single molecule localization microscopy: why optimization of sample preparation protocols matters. *Sci Rep*, 5:7924, 2015.
- [108] Rochester Insitute of Technology. Circular hough transform, <https://www.cis.rit.edu/class/simg782.old/talkhough/houghleccircles.html>, visited on 29.07.2015.
- [109] M. Ovesny et al. Thunderstorm: a comprehensive imagej plug-in for palm and storm data analysis and super-resolution imaging. *Bioinformatics*, 30:2389–90, 2014.
- [110] M. Ovesny et al. Thunderstorm: a comprehensive imagej plugin for palm and storm data analysis and super-resolution imaging - methodology and algorithms.
- [111] T. Quan et al. Localization capability and limitation of electron-multiplying charge-coupled, scientific complementary metal-oxide semiconductor, and charge-coupled devices for superresolution imaging. *J Biomed Opt*, 15, 2010.
- [112] T. Quan et al. Errata: Localization capability and limitation of electron-multiplying charge-coupled, scientific complementary metal-oxide semiconductor, and charge-coupled devices for superresolution imaging. *Journal of Biomedical Optics*, 17, 2012.
- [113] A. Reismann. *Einzelmolekulare Analyse des MDR 1-medierten Substrattransportes*. Thesis, 2013.

- [114] P. Annibale et al. Photoactivatable fluorescent protein meos2 displays repeated photoactivation after a long-lived dark state in the red photoconverted form. *J Phys Chem Lett*, 1:1506–10, 2010.
- [115] P. Annibale et al. Quantitative photo activated localization microscopy: Unraveling the effects of photoblinking. *PLoS ONE*, 6, 2011.
- [116] P. Annibale et al. Identification of clustering artifacts in photoactivated localization microscopy. *Nat Methods*, 8:527–8, 2011.
- [117] P. M. Dixon. Ripley’s k function. *Encyclopedia of Environmetrics*, 3:1796–803, 2002.
- [118] M. A. Kiskowski et al. On the use of ripley’s k-function and its derivatives to analyze domain size. *Biophys J*, 97:1095–103, 2009.
- [119] D. Sage et al. Quantitative evaluation of software packages for single-molecule localization microscopy. *Nat Methods*, 2015.
- [120] J. J. Illingworth and P. Anton van der Merwe. Dissecting t-cell activation with high-resolution live-cell microscopy. *Immunology*, 135:198–206, 2012.
- [121] J. Sloan-Lancaster et al. Zap-70 association with t cell receptor  $\zeta$ : Fluorescence imaging of dynamic changes upon cellular stimulation. *J Cell Bio*, 143:613–24, 1998.
- [122] T. Brocker and K. Karjalainen. Signals through t cell receptor- $\zeta$  chain alone are insufficient to prime resting t lymphocytes. *J Exp Med*, 181:1653–59, 1995.
- [123] O. Dushek et al. Effects of intracellular calcium and actin cytoskeleton on tcr mobility measured by fluorescence recovery. *PLoS One*, 3:3913, 2008.
- [124] A. C. Chan et al. The  $\zeta$  chain is associated with a tyrosine kinase and upon t-cell antigen receptor stimulation associates with zap-70, a 70-kda tyrosine phosphoprotein. *Proc Natl Acad Sci U S A*, 88:9166–70, 1991.
- [125] R. Renthal. Buried water molecules in helical transmembrane proteins. *Protein Sci*, 17:293–8, 2008.
- [126] A. A. Petruk et al. The structure of the cd3  $\zeta\zeta$  transmembrane dimer in popc and raft-like lipid bilayer: a molecular dynamics study. *Biochim Biophys Acta*, 1828:2637–45, 2013.

- [127] S. H. Lee et al. Counting single photoactivatable fluorescent molecules by photoactivated localization microscopy (palm). *Proc Natl Acad Sci U S A*, 109:17436–41, 2012.
- [128] T. Yokosuka et al. Newly generated t cell receptor microclusters initiate and sustain t cell activation by recruitment of zap70 and slp-76. *Nat Immunol*, 6:1253–62, 2005.
- [129] J. Gunzenhauser et al. Quantitative super-resolution imaging reveals protein stoichiometry and nanoscale morphology of assembling hiv-gag virions. *Nano Lett*, 12:4705–10, 2012.
- [130] E. M. Puchner et al. Counting molecules in single organelles with superresolution microscopy allows tracking of the endosome maturation trajectory. *Proc Natl Acad Sci U S A*, 110:16015–20, 2013.
- [131] X. Nan et al. Single-molecule superresolution imaging allows quantitative analysis of raf multimer formation and signaling. *Proc Natl Acad Sci U S A*, 110:18519–24, 2013.
- [132] N. Durisic et al. Single-molecule evaluation of fluorescent protein photoactivation efficiency using an in vivo nanotemplate. *Nat Methods*, 11:156–62, 2014.
- [133] D. J. Williamson et al. Pre-existing clusters of the adaptor lat do not participate in early t cell signaling events. *Nat Immunol*, 12:655–62, 2011.
- [134] M. Jinek et al. A programmable dual-rna-guided dna endonuclease in adaptive bacterial immunity. *Science*, 337:816–21, 2012.
- [135] M. Ratz et al. Crispr/cas9-mediated endogenous protein tagging for resolt super-resolution microscopy of living human cells. *Sci Rep*, 5:9592, 2015.
- [136] M. Schwarzenbacher et al. Micropatterning for quantitative analysis of protein-protein interactions in living cells. *Nat Methods*, 5:1053–60, 2008.
- [137] A. M. Lipp et al. Lck mediates signal transmission from cd59 to the tcr/cd3 pathway in jurkat t cells. *PLoS One*, 9, 2014.
- [138] P. Sengupta and J. Lippincott-Schwartz. Quantitative analysis of photoactivated localization microscopy (palm) datasets using pair-correlation analysis. *Bioessays*, 34:396–405, 2012.

- [139] S. L. Veatch et al. Correlation functions quantify super-resolution images and estimate apparent clustering due to over-counting. *PLoS One*, 7, 2012.